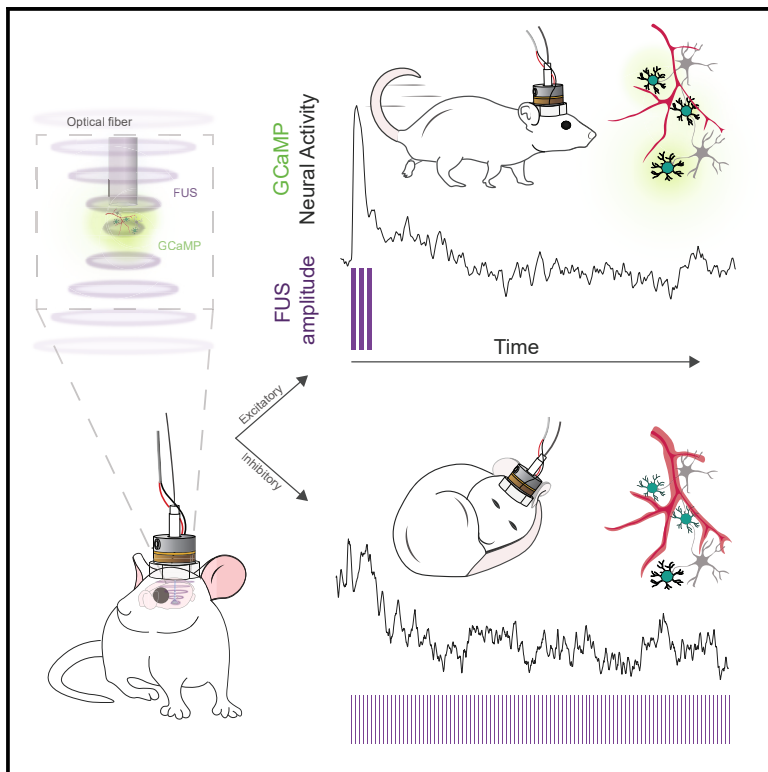


## Optimized ultrasound neuromodulation for non-invasive control of behavior and physiology

### Graphical abstract



### Authors

Keith R. Murphy, Jordan S. Farrell,  
Jonas Bendig, ..., Kim Butts-Pauly,  
Ivan Soltesz, Luis de Lecea

### Correspondence

llecea@stanford.edu

### In brief

The field of focused ultrasound (FUS) neuromodulation is undergoing rapid growth but is limited by our understanding of effective waveform parameters and cell-type effects. Murphy et al. combine deep-brain optical readouts with FUS technology to uncover waveforms for inducing powerful, bidirectional neuromodulation across a collection of therapeutically important brain cell types.

### Highlights

- Optimal ultrasound neuromodulation parameters generalize across neuronal cell types
- Distinct parameters for excitation and inhibition are identified
- Targeted stimulation induces site-specific behavioral changes
- COX2-dependent vasoconstriction and brain cooling occur with excitatory protocols



## NeuroResource

# Optimized ultrasound neuromodulation for non-invasive control of behavior and physiology

Keith R. Murphy,<sup>1</sup> Jordan S. Farrell,<sup>2,3,4,5</sup> Jonas Bendig,<sup>6</sup> Anish Mitra,<sup>1</sup> Charlotte Luff,<sup>1</sup> Ina A. Stelzer,<sup>7</sup> Hiroshi Yamaguchi,<sup>1,9</sup> Christopher C. Angelakos,<sup>1</sup> Mihyun Choi,<sup>8</sup> Wenjie Bian,<sup>1,10,11</sup> Tommaso Dilanni,<sup>8,12</sup> Esther Martinez Pujol,<sup>1</sup> Noa Matosevich,<sup>1,13</sup> Raag Airan,<sup>8</sup> Brice Gaudillière,<sup>6</sup> Elisa E. Konofagou,<sup>6</sup> Kim Butts-Pauly,<sup>8</sup> Ivan Soltesz,<sup>2</sup> and Luis de Lecea<sup>1,14,\*</sup>

<sup>1</sup>Department of Psychiatry and Behavioral Sciences, Stanford University, Stanford, CA, USA

<sup>2</sup>Department of Neurosurgery, Stanford University, Stanford, CA, USA

<sup>3</sup>Department of Neurology, Harvard Medical School, Boston, MA, USA

<sup>4</sup>Rosamund Stone Zander Translational Neuroscience Center, Boston Children's Hospital, Boston, MA, USA

<sup>5</sup>F.M. Kirby Neurobiology Center, Harvard Medical School, Boston, MA, USA

<sup>6</sup>Department of Biomedical Engineering, Columbia University, New York, NY, USA

<sup>7</sup>Department of Anesthesia, Stanford University, Stanford, CA, USA

<sup>8</sup>Department of Radiology, Stanford University, Stanford, CA, USA

<sup>9</sup>Department of Neuroscience, Nagoya University, Nagoya, Japan

<sup>10</sup>Westlake Laboratory of Life Sciences and Biomedicine, Hangzhou, Zhejiang, China

<sup>11</sup>School of Life Sciences, Westlake University, Hangzhou, Zhejiang, China

<sup>12</sup>Department of Psychiatry and Behavioral Sciences, University of California, San Francisco, San Francisco, CA, USA

<sup>13</sup>Sagol School of Neuroscience, Tel Aviv University, Tel Aviv, Israel

<sup>14</sup>Lead contact

\*Correspondence: llecea@stanford.edu

<https://doi.org/10.1016/j.neuron.2024.07.002>

## SUMMARY

Focused ultrasound can non-invasively modulate neural activity, but whether effective stimulation parameters generalize across brain regions and cell types remains unknown. We used focused ultrasound coupled with fiber photometry to identify optimal neuromodulation parameters for four different arousal centers of the brain in an effort to yield overt changes in behavior. Applying coordinate descent, we found that optimal parameters for excitation or inhibition are highly distinct, the effects of which are generally conserved across brain regions and cell types. Optimized stimulations induced clear, target-specific behavioral effects, whereas non-optimized protocols of equivalent energy resulted in substantially less or no change in behavior. These outcomes were independent of auditory confounds and, contrary to expectation, accompanied by a cyclooxygenase-dependent and prolonged reduction in local blood flow and temperature with brain-region-specific scaling. These findings demonstrate that carefully tuned and targeted ultrasound can exhibit powerful effects on complex behavior and physiology.

## INTRODUCTION

Focused ultrasound (FUS) can be used for non-invasive modulation of brain activity at the millimeter scale in even the deepest brain areas, allowing for unprecedented access to deep-brain neural circuits.<sup>1–3</sup> To date, FUS has shown efficacy in the modulation of both neuronal and non-neuronal cell types, influencing a diversity of physiological and pathological states.<sup>3–23</sup> Given the expansive brain access availed through FUS, a breadth of cell types and areas are being actively researched. While stimulation protocol features found to be efficacious in discrete brain targets are being broadly applied across experimental paradigms,<sup>1,24,25</sup> the generalizability of

parameter efficacy across brain areas remains largely unknown. This is further obscured by the fact that the effective waveform parameter space has only been scarcely examined. To systematically address these questions, new tools and approaches are required.

Single-pulse parametric studies have found that intensity and duration are directly related to neuronal excitation, with general consensus across experimental conditions.<sup>10,16,26–31</sup> More sophisticated pulsing schemes, typical of human research applications, are also being examined in animal models.<sup>29,32,33</sup> In parallel to parametric studies, the differential effects of FUS on various cell types is also under active investigation.<sup>34–36</sup> In mice, distinct directional and temporal effects have been observed between



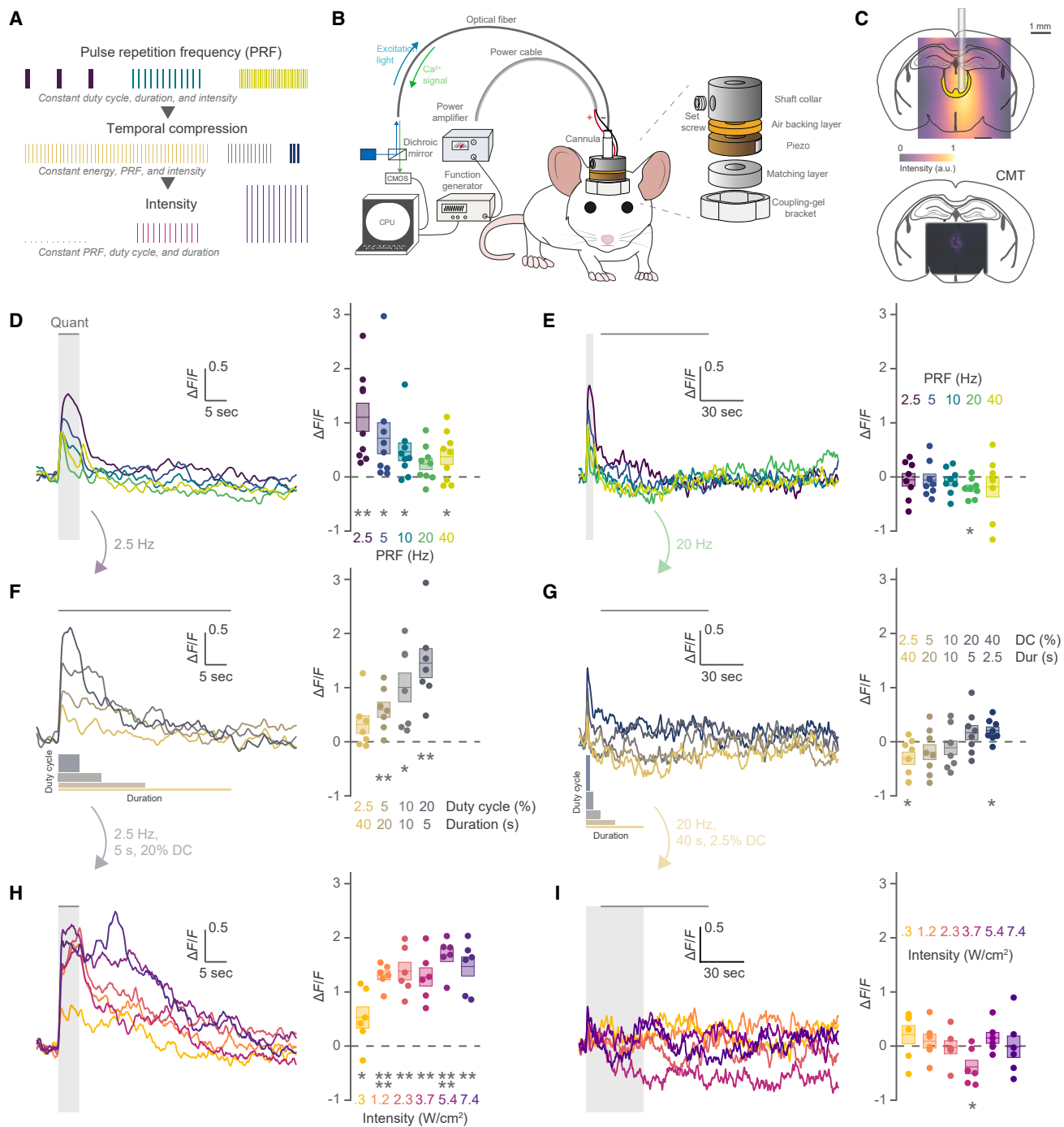


**Figure 1.** Stepwise parametric sweeps of ultrasound features reveal bidirectional manipulation of the midline thalamic nuclei

(A) Illustration of parametric features examined at each step.

(B) Overlay of FUS intensity field on intended CMT target area accompanied by a fluorescence image overlay of CMT GCaMP6s expression.

(C) Overlay of FUS intensity fields and fluorescence images of GCaMP6s-expressing CAMKII+ CMT neurons.

(D) CMT calcium responses during FUS stimulus as functions of ultrasound PRF. The gray line (Quant) represents the period over which the response was quantified for all line plots (bars represent mean  $\pm$  SEM, and circles represent animals for all plots,  $n = 9$  mice, repeated-measures ANOVA  $p = 0.007$ , one-sample t test; \* $p < 0.05$ , \*\* $p < 0.01$ ).

(E) CMT calcium responses during post-FUS period (10–85 s post stimulus onset) as functions of ultrasound PRF ( $n = 9$  mice, one-sample t test; \* $p = 0.038$ ).

(F) CMT calcium responses during stimulus (0–40 s post stimulus onset) as functions of 2.5 Hz temporal compression ( $n = 7$  mice, repeated-measures ANOVA  $p = 0.0098$ , one-sample t test; \* $p < 0.05$ , \*\* $p < 0.01$ ).

(legend continued on next page)

neighboring cell types,<sup>16,32</sup> which may be due to local inhibition.<sup>34</sup> Similarly, astrocytes may be more sensitive to FUS and may enhance or drive local neuronal activity.<sup>10,31</sup> More recently, cell-type specificity has been examined in the central nervous system of humans, with differential GABA release across cortical regions,<sup>37</sup> and in non-human primates, where fMRI blood-oxygen-level-dependent response differed across five distinct brain regions.<sup>38</sup> Together, these prior reports point to different parameter sensitivity across cell types, which may be explained by genetically encoded FUS sensitivity.<sup>30,39,40</sup> However, the existence of a broadly excitatory or inhibitory feature space remains to be determined.

Here, we applied a coordinate descent method for multi-parametric optimization of neural activity change across four distinct cell populations. We selected arousal centers with the goal of producing clearly observable changes in behavior—a strategy taken in the earliest demonstration of optogenetics in mice.<sup>41</sup> We found that the optimized protocols elicit rapid and evident changes in behavior that are specific to each target and are largely absent when applying non-optimized protocols. We further investigate the physiological impacts of these protocols and show changes in focal brain temperature and blood volume, indicating powerful neuromodulation and protracted vascular effects. This proof-of-concept study provides a platform surveying the available FUS parameters to optimize for specific cell types using openly available tools, which can be broadly implemented across labs with varying research questions as a critical step toward translation of mechanistically guided neuromodulation.

## RESULTS

### Optimizing excitation and inhibition of deep-brain arousal centers

For our parametric search, we chose three ultrasound features with substantial heterogeneity across ultrasound neuromodulation studies (Figure 1A). We first examined pulse repetition frequency (PRF), which plays a critical role in neuromodulation across modalities such as deep-brain, optogenetic, and transcranial magnetic stimulation.<sup>42–45</sup> We next examined temporal compression, which inversely varies pulse duration and pulse train duty cycle while keeping total power delivery constant. For instance, a 2-fold compression would be achieved by reducing duration by half and doubling duty cycle. Varying this feature may be used to limit the tissue heating associated with ultrasound absorption. For the final step, we examined spatial-peak pulse-average intensity (ISPPA), which is a common metric of energy delivered and is causally related to tissue displacement, heating, and ion channel opening in the membrane.<sup>28,46</sup> Given the vast parametric space available, we used a feed-forward coordinate descent strategy in which optima for each parameter are successively derived independently, while all

other features remain constant. Each optimal coordinate was then passed on as a constant for examination of the subsequent parameter (Figure 1A; Table S1). While this method is prone to identifying local maxima, it allows rapid evaluation of a single axis without requiring extensive search of high-dimensional space.<sup>47</sup>

We first examined  $\text{Ca}^{2+}$  calmodulin-dependent protein kinase II-positive (CAMKII+) excitatory neurons of the central medial thalamus (CMT), a cell type known to play a role in cortical rhythm entrainment with the potential to impact sleep and epilepsy.<sup>48–50</sup> GCaMP6s was virally expressed under the CAMKII promoter in the CMT, and an optical fiber was implanted immediately dorsal to it (Figures 1B and 1C). To deliver FUS to the target area, we used a mountable ring transducer developed for freely behaving animals (Figure 1B)<sup>16</sup> at an operating frequency of 550 kHz, which is well within the frequency range used in human clinical applications. The field full-width half-maximum was ~2.3 mm lateral (wide) and 7.2 mm axial (long) with the focal peak at ~6 mm from the transducer face (Figure S1), not accounting for standing waves, which will affect the field intensity heterogeneously. Ultrasound was pulsed with 5 different PRFs ranging from 2.5 to 40 Hz while maintaining a fixed pulse train duty cycle of 20%, an intensity of 3.7 W/cm<sup>2</sup>, and a pulse train of 5 s. We found that lower PRFs with longer individual pulse durations significantly increased neuronal activity detectable in the GCaMP6s signal during the stimulation period (Q1; 0–5 s post stimulation onset), with the largest increase at 2.5 Hz (Figure 1D). We quantified post-stimulation inhibition using a time window inclusive of any observed decrease in neural activity below baseline across the animal-averaged response (10–85 s post stimulation onset). During this period, we found a non-monotonic response curve of neural inhibition to PRF where 20 Hz pulsing significantly suppressed activity (Figure 1E).

With a PRF of 2.5 Hz selected for excitation and 20 Hz for inhibition, we then passed these PRF parameters onto the temporal compression step in which the duration of pulsing was incrementally increased while duty cycle decreased, such that total power delivery was held constant (Figure 1A). For stimulus-locked effects, we quantified the response over the longest duration (0–40 s post stimulation onset) to be inclusive of all protocol stimulus periods. We found that compression enhanced excitation of the 2.5 Hz excitatory parameter (Figure 1F, maximal excitation at 5 s, 20% duty cycle), whereas decreasing compression with the 20 Hz pulsing led to the greatest inhibition (Figure 1G, 40 s 2.5% duty cycle). Finally, we optimized power by incrementally increasing the spatial peak intensity from 0.3 to 7.4 W/cm<sup>2</sup>. Excitation during the stimulus was achieved even at lower intensities, with peak excitation at 5.4 W/cm<sup>2</sup> (Figure 1H). In contrast, examination of the inhibitory protocol intensity showed significant post-stimulus suppression only at 3.7 W/cm<sup>2</sup> (Figure 1I). Importantly, floor effects may lower the resolution of inhibitory protocols relative to baseline.

(G) CMT calcium responses during post-FUS period as functions of ultrasound 20 Hz temporal compression ( $n = 8$  mice, one-sample t test; \* $p < 0.05$ ).

(H) CMT calcium responses during stimulus as functions of 2.5 Hz, 5 s compressed ultrasound intensity ( $n = 6$  mice, repeated-measures ANOVA  $p = 0.0007$ , one-sample t test; \* $p < 0.05$ , \*\* $p < 0.01$ , \*\*\* $p < 0.0001$ ).

(I) CMT calcium responses during post-FUS period as functions of ultrasound 20 Hz, 40 s compressed ultrasound intensity ( $n = 6$  mice, one-sample t test; \* $p < 0.05$ ).

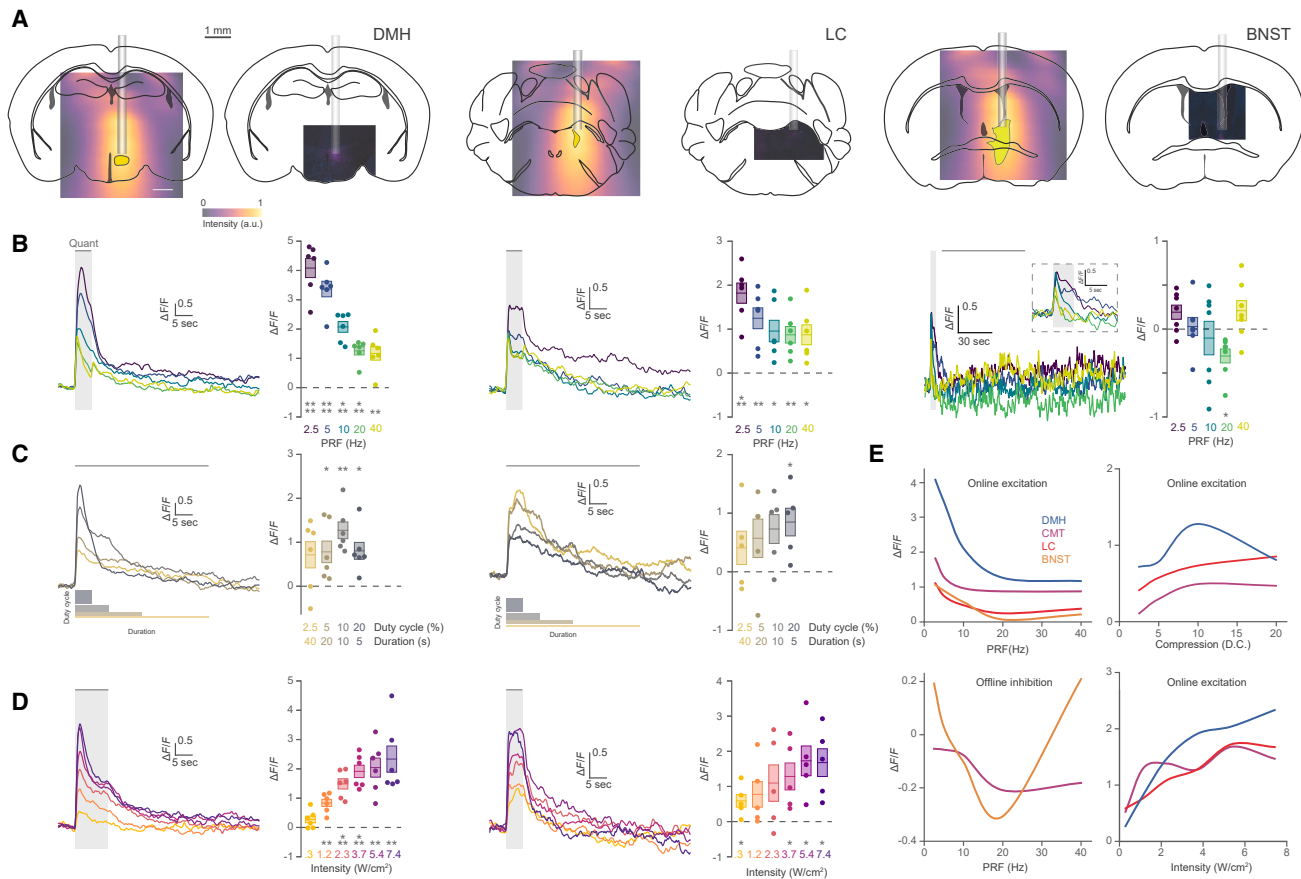


**Figure 2. Stepwise parametric sweeps of variant cell types reveal conserved and variant waveform optima**

- (A) Overlay of FUS intensity fields and fluorescence images of the GCaMP6s-expressing DMH, LC, and BNST target areas.
- (B) Time series and time-averaged calcium activity during FUS stimulus as functions of ultrasound PRF for the DMH (left,  $n = 6$  mice, bars represent mean  $\pm$  SEM, and circles represent animals for all plots, repeated-measures ANOVA  $p < 0.0001$ , one-sample t test; \* $p < 0.05$ , \*\* $p < 0.01$ , \*\*\* $p < 0.001$ , \*\*\*\* $p < 0.0001$ ), LC (middle,  $n = 6$  mice, repeated-measures ANOVA  $p = 0.026$ ), and BNST (right,  $n = 7$ , one-sample t test; \* $p = 0.012$ ).
- (C) Calcium responses during stimulus as functions of 2.5 Hz temporal compressed FUS for the DMH (one-sample t test; \* $p < 0.05$ , \*\* $p < 0.01$ ) and LC.
- (D) Calcium responses during stimulus as functions of 2.5 Hz, 5 s compressed FUS for the DMH (repeated-measures ANOVA  $p = 0.0074$ , one-sample t test; \*\* $p < 0.01$ , \*\*\* $p < 0.001$ ) and LC (one-sample t test; \* $p < 0.05$ ).
- (E) Spline fits of  $\Delta F/F$  versus each feature examined across cell types examined.

### Optimal parameters are heterogeneous across brain areas and cell types

We next examined whether the optimal feature space identified in the CAMKII+ CMT neurons would be conserved across other arousal-related cell types. We chose the dorsomedial hypothalamic (DMH) GABAergic neurons, locus coeruleus (LC) noradrenergic neurons, and GABAergic neurons of the bed nucleus of the stria terminalis (BNST) (Figure 2A) because previous works suggest that they are FUS sensitive and that their activation elicits arousal-related behaviors.<sup>8,16,51,52</sup> A DLX-promoter-driven GCaMP6s was used for the examination of DMH or BNST GABA-positive neurons and a tyrosine hydroxylase (TH) promoter mouse strain (TH-flpO+) with a flp-dependent GCaMP6s viral element was used to examine TH+ LC neurons (Figure 2A). DLX+ DMH and TH+ LC neurons showed robust stimulus-locked response to all PRFs, with the largest increases at lower PRFs, similar to the CMT response profile (Figure 2B, left and middle). BNST neurons did not show activation at any PRF (Figure S2A).

but did undergo a significant decrease during the post-stimulus period at 20 Hz stimulation, similar to the CMT (Figure 2B, right). A two-way ANOVA of response during the FUS stimulus showed that there was a significant overall effect of PRF across brain regions ( $F(4, 120) = 18.85, p < 0.0001$ ), that brain regions respond differently ( $F(3, 120) = 51.71, p < 0.0001$ ), and that a significant interaction between PRF and brain region exists ( $F(12, 120) = 2.995, p < 0.01$ ).

In examining compression, LC neurons showed greatest excitation at 5-s 20% duty cycle (D.C.), matching the optimal CMT waveform (Figure 2C, middle.). In contrast, we found that the DMH responded maximally at 10-s, 10% D.C. compression (Figure 2C, left). A two-way ANOVA of response during the stimulus window (0–40 s post stimulation) across brain regions showed that there was no significant overall effect of duration ( $F(3, 60) = 1.55, p = 0.211$ ) but significant differences across brain regions ( $F(2, 60) = 5.49, p = 0.006$ ), indicating that duration optimization varies significantly across areas. BNST neurons did not

show significant suppression at any compression of the 20 Hz protocol and were not passed onto the intensity step of examination (Figure S2B). Both LC and DMH neurons showed increased response during stimulation with increasing intensity (Figure 2D). In general, similar trends for feature response profiles were found across the various cell types examined, with different optimal parameters and clear differences in response magnitude (Figure 2E). Despite previous findings that inhibitory interneurons may inhibit their excitatory outputs,<sup>16,34</sup> we found that CAMKII+ neurons of the paraventricular nucleus (PVN), which are in close proximity to the DMH (~0.4 mm) and receive inhibitory inputs from the GABAergic DLX+ neurons,<sup>53,54</sup> were still excited by the same DMH-targeted stimulus (Figures S3A and S3B). Furthermore, the FUS-induced neural response was larger than that generated by a very loud 16 kHz, 96 dB tone with the same envelope played in the animal's environment (Figures S6C and S6D). These findings indicate that the optimized ultrasound protocol not only overrides local inhibitory inputs but also produces larger excitation than salient external stimuli.<sup>55</sup>

Previous works have clearly demonstrated that FUS has audible components that can result in non-specific activation of some brain areas through bone and fluid conductive hearing.<sup>56–60</sup> To examine the extent to which neural response was due to non-specific effects arising from peripheral auditory or tactile stimulation, we used the z axis adjustability of the photometry-coupled ultrasound (PhoCUS) probe to move the focus 3 mm dorsal to each target. This places the focal peak closer to cortical areas and skull bone, which should result in greater shear-wave propagation to the cochlea and louder audible sound.<sup>60</sup> With the off-target focus, the cell types showed reduced response without significant modulation at any intensity, suggesting that audition is not playing a dominant role in the observed response (Figures S4A–S4D). Intriguingly, the CMT response was lower than expected for partial pressure exposure, which may suggest the presence of standing waves creating low-pressure nodes at the focus or inhibition of the CMT by off-target networked areas. Moreover, simulated audibility of the ultrasound stimulation did not correlate with the neuronal response (Figures S4E–S4G). However, simulations were based on a brain with null viscosity and a skull absent an optical fiber implant, which may interfere with shear-wave propagation and alter FUS audibility.<sup>60</sup>

#### FUS induces clear protocol and target-specific behavioral effects

The thalamus, hypothalamus, and LC are all linked to varying levels of consciousness,<sup>48,61</sup> anxiety,<sup>62</sup> and locomotion,<sup>8,16,51,52,62,63</sup> which often manifest in visible changes in behavior easily replicated across laboratories. To examine whether differences in neuromodulation corresponded with overt behavioral changes, we coupled neural measurements with machine vision ethological monitoring. We used automated video tracking to quantify changes in head motion, walking, and body shape while stimulating the various brain targets at optimal excitation or inhibition (Figure 3A). Given the bidirectional CMT response obtained with different protocols, we asked whether bidirectional behavioral manipulation could also be achieved. Targeting the CMT with the

CAMKII+-optimized excitatory waveform caused an increase in head motion during the stimulus (Figure 3B), consistent with findings that the CMT stimulation promotes arousal.<sup>48,49</sup> In contrast, we observed a significant decrease in head motion when applying the inhibitory protocol during the dark phase (Figure 3B). Since changes in head motion were not observed when CMT-optimized inhibitory parameters were applied to the BNST or LC (Figure 3B), these results demonstrate that optimizing parameters for activation and inhibition of local cell types can achieve selective and bidirectional control of behavior.

When targeting the DMH, stimulation produced a clear and immediate increase in walking that extended beyond the stimulation period (Figure 3C; Video S1). Animals also exhibited a rapid and transient increase in stretch attend posture (SAP), a behavior that manifests during increased states of anxiety<sup>64</sup> (Figure 3D). Even when the animals were not walking, head motion was significantly increased (Figure 3E), indicating some level of arousal and dynamic investigation of their environment.<sup>65</sup> To examine whether the optical optimizations had any bearing on behavioral outcomes, we stimulated the DMH with the same intensity and duty cycle but with a suboptimal PRF of 20 Hz that results in less activation of local neurons (Figure 2B). This ostensibly subtle waveform difference eliminated significant walking induction (Figure 3C). Although suboptimal stimulation still increased SAP, both SAP and head speed were significantly less during the suboptimal protocol in comparison to the optimized waveform (Figures 3D and 3E). In contrast, the DMH-optimized protocol targeted to either the BNST or LC did not result in any significant increases in walking, SAP, or head motion (Figure 3C), suggesting that these behavioral effects are both target and waveform specific. Repeated FUS stimulation of the DMH did not lead to a significant reduction in successive neuronal activation or walking response (Figures S5A and S5B). However, CMT neural activity and behavioral response significantly changed, with latter trials being significantly lower than the first trial (Figures S5C and S5D). To assess whether the optical fiber was necessary for FUS-induced behavioral changes, we mounted cannulas without optical fiber implants and found that behavioral response was maintained (Figure S6). Importantly, the behavior was eliminated by moving the focus 3 mm posterior to the target, further demonstrating the specificity of brain area targeted for behavioral intervention (Figure S6). To compare FUS stimulation to another neuromodulatory modality, we performed optogenetic stimulation of the DMH using pan-neuronal expression of ChRmine below the optical fiber (Figure S6D). 10 Hz pulsing elicited a similar increase in walking and head speed, confirming that stimulation of the hypothalamus can elicit locomotion (Figures S7E and S7F). Intriguingly, SAP was not significantly increased (Figure S7G), suggesting that the broader ultrasound field might engage SAP through a neighboring hypothalamic brain area.

Hypocretin neurons of the lateral hypothalamus (LH), a region positioned ~0.7 mm lateral to the DMH, have previously been implicated in arousal and the behavioral manifestation of stress and anxiety.<sup>66</sup> Thus, the focus was positioned onto the LH while recording hypocretin neuron activity and behavior in Hcrt-cre animals (Figure 4A). We found that stimulation of the LH increased walking only during FUS stimulation, compared to the DMH

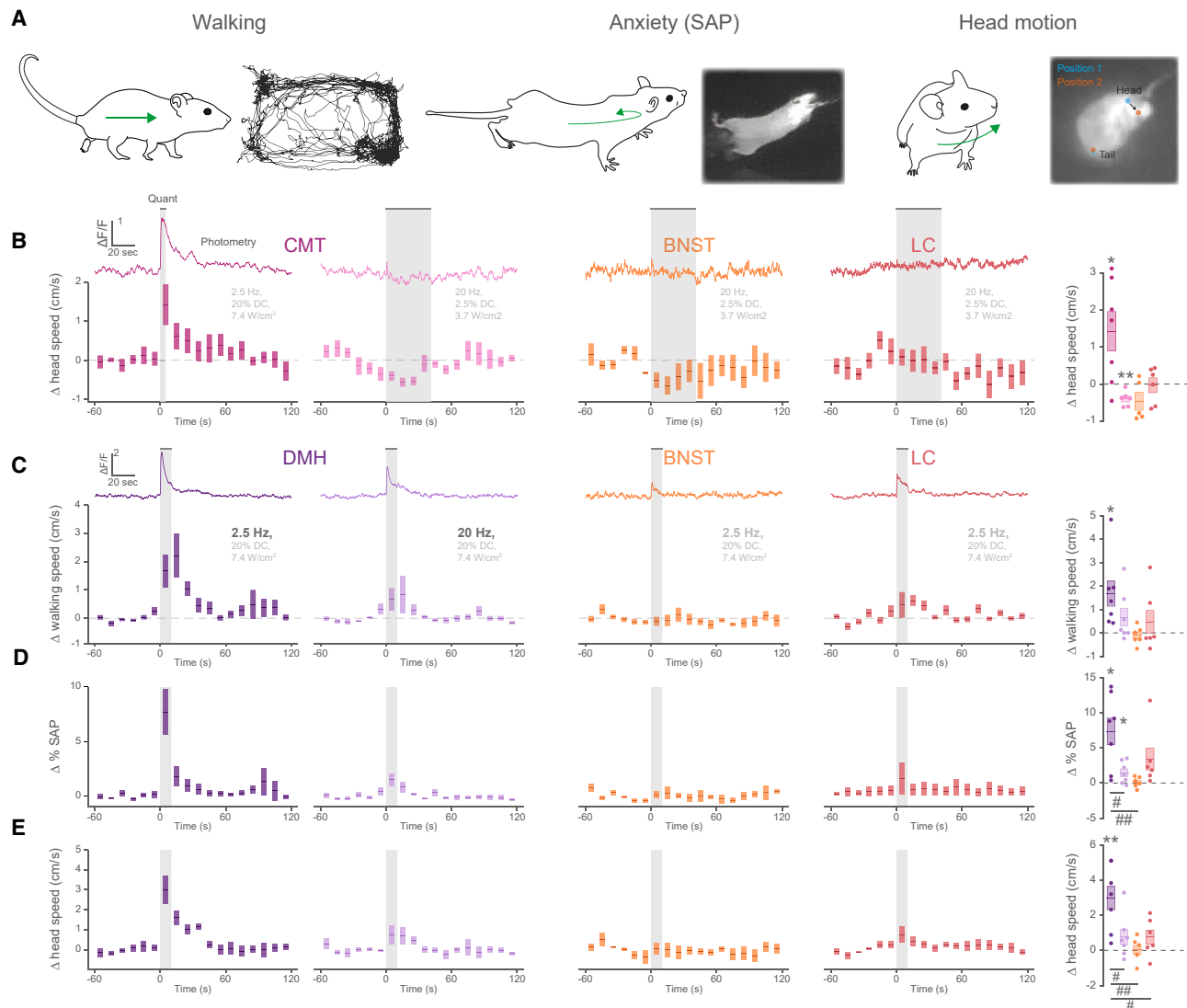


**Figure 3. Optimized FUS protocols induction of distinct walking and head motion behavior**

(A) Illustration of behaviors examined using overhead infrared image tracking.

(B) Time series of change in head speed with varying target and FUS waveform stimulation ( $\Delta$  relative to pre-stimuli baseline, shaded gray area represents stimuli period, bars represent mean  $\pm$  SEM, 10 s bins). Associated GCaMP6s photometry recordings are shown for all behavioral time series (trace represents 10-trial average). Individual animal means during stimuli (“Quant” period, gray line) are collated to the right of the time series ( $n = 6\text{--}7$  mice per group, bars represent mean  $\pm$  SEM, and circles represent animals for all plots, one-sample t test; \*\*,  $p < 0.01$ . Groups are compared using a one-way ANOVA with Bonferroni correction; # $p < 0.05$ , ## $p < 0.01$ ).

(C-E) Time series of change in body speed (C), stretch attend posture (D), and head speed (E) with varying target and FUS waveform stimulation ( $\Delta$  relative to pre-stimuli baseline, shaded gray area represents stimuli period, bars represent mean  $\pm$  SEM, 10 s bins). Individual animal means during FUS stimulation are collated to the right of the time series ( $n = 6\text{--}7$  mice per group, one-sample t test; \*,  $p < 0.05$ , \*\* $p < 0.01$ . Groups are compared using a one-way ANOVA with Bonferroni correction; # $p < 0.05$ , ## $p < 0.01$ ).

stimulation, which increased walking for up to 30 s after the stimulus onset (Figure 4B). In contrast, LH stimulation resulted in extended SAP, lasting up to 40 s following stimulation onset, while DMH stimulation only increased SAP during the stimulus (Figure 4B). A two-way ANOVA of response over time when targeting the two different brain areas indicated significant effects of time since stimulation onset ( $F(17, 234) = 5.66, p < 0.0001$ )

and brain region ( $F(1, 234) = 16.57, p < 0.0001$ ). This suggests that walking and SAP arise from independent neuromodulated sites within the hypothalamus. Intriguingly, DMH stimulation led to a significantly shorter time to failure during motivated walking on the rotarod task (Figure 4D; Video S3), whereas stimulation of the LH did not change time to failure. Furthermore, we found a strong correlation between each animal’s change in

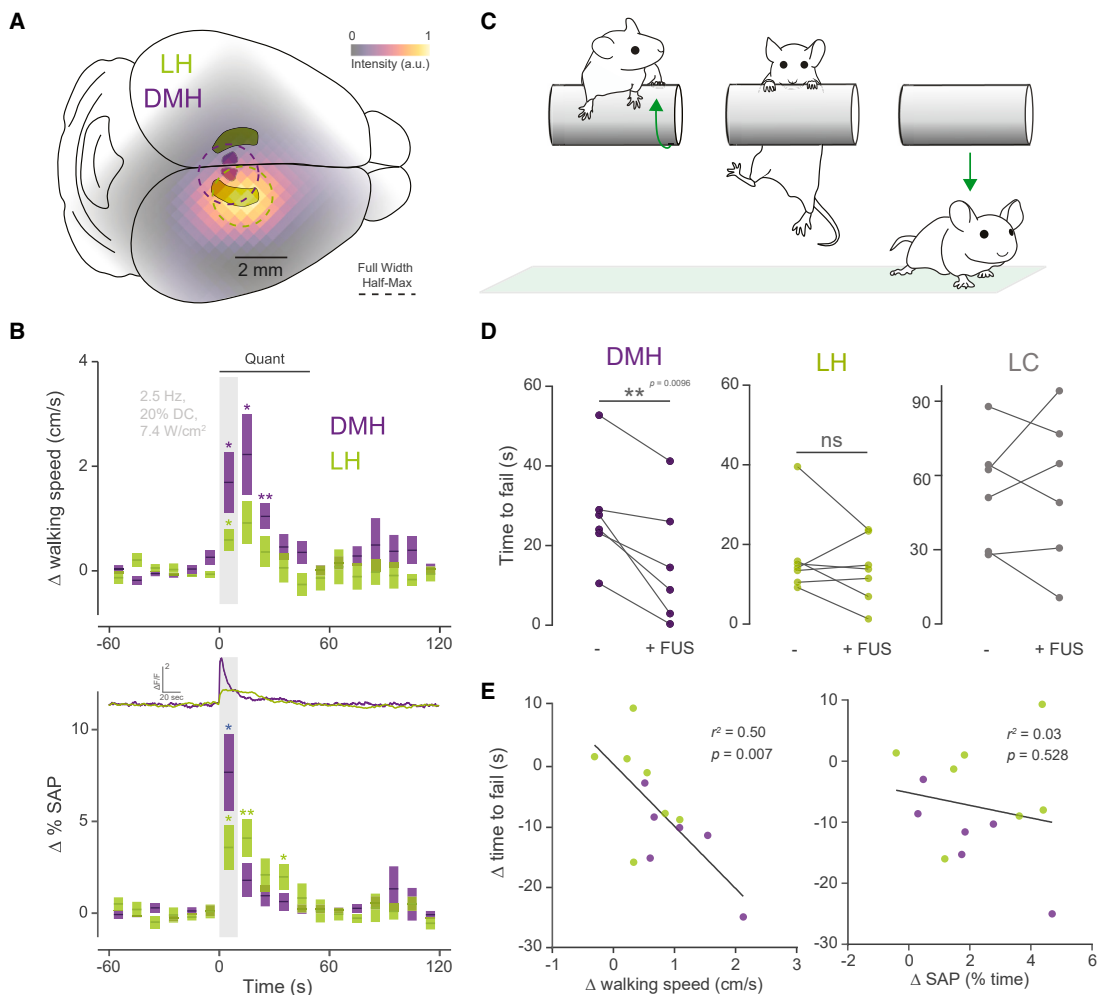


**Figure 4. Hypothalamic subregions produce differential behavioral response to FUS stimulation**

(A) Horizontal plane view of the mouse brain with dorsomedial and lateral hypothalamic subregions. The circle approximates the lateral full-width half-maximum boundaries when targeting either region (green, lateral hypothalamus; blue, dorsomedial hypothalamus).

(B) Overlaid time series of change in walking speed and stretch attend posture when stimulating either of the hypothalamic subregions ( $n = 6\text{--}7$  mice, DMH data repeated from Figures 5B and 5C, bars represent mean  $\pm$  SEM for all plots, one-sample t test; \* $p < 0.05$ , \*\* $p < 0.01$ ; Q1: 0–50 s post stimulation).

(C) Illustration of rotarod task where time is measured between FUS onset and task failure.

(D) Change in time to failure on the rotarod task with and without FUS stimulation applied to either of the hypothalamic subregions or the LC (circles represent individual animals for all plots, paired two-tailed t test; \*\* $p < 0.01$ ).

(E) Linear correlation of freely behaving motion changes during the stimulus (Quant, B) and change in time to failure with and without FUS stimulation (D) (Pearson correlation, DMH, two-tailed  $p = 0.0066$ ; LH, two-tailed  $p = 0.5275$ ). The quantified period was chosen to be inclusive of all rotarod failure times (0–50 s post stimulus onset).

rotarod failure time and their free field walking but found no correlation with their change in SAP (Figure 4E). This interruption of walking behavior was not observed during LC stimulation, highlighting the specificity of this response to the hypothalamic locomotor region (Figure 4D).

#### FUS induces local brain cooling and cyclooxygenase-dependent vasoconstriction

Because the excitatory protocols more rapidly deposit energy in the brain, we questioned whether FUS-induced temperature increases might explain differences in neuromodulation, as observed in various neural structures.<sup>67,68</sup> By replacing the opti-

cal fiber with a thermocouple, we monitored local brain temperature at the ultrasound focus and immediately beneath the skull when targeting the CMT (Figure 5A). In contrast to the generally accepted notion that FUS increases tissue temperature, we found a decrease at the focus by nearly 1°C (Figure 5B). The excitatory and inhibitory protocols increased temperature immediately above the cortex by up to 1.49°C and 0.72°C, respectively, since the skull is highly absorbent of ultrasound waves and the probe itself produces heat (Figure 5D). Blood flow can act as a convective pump to distribute heat around the brain, often used as a term in bioheat equations for FUS heating.<sup>69,70</sup> To examine whether blood volume changed at the focus, we

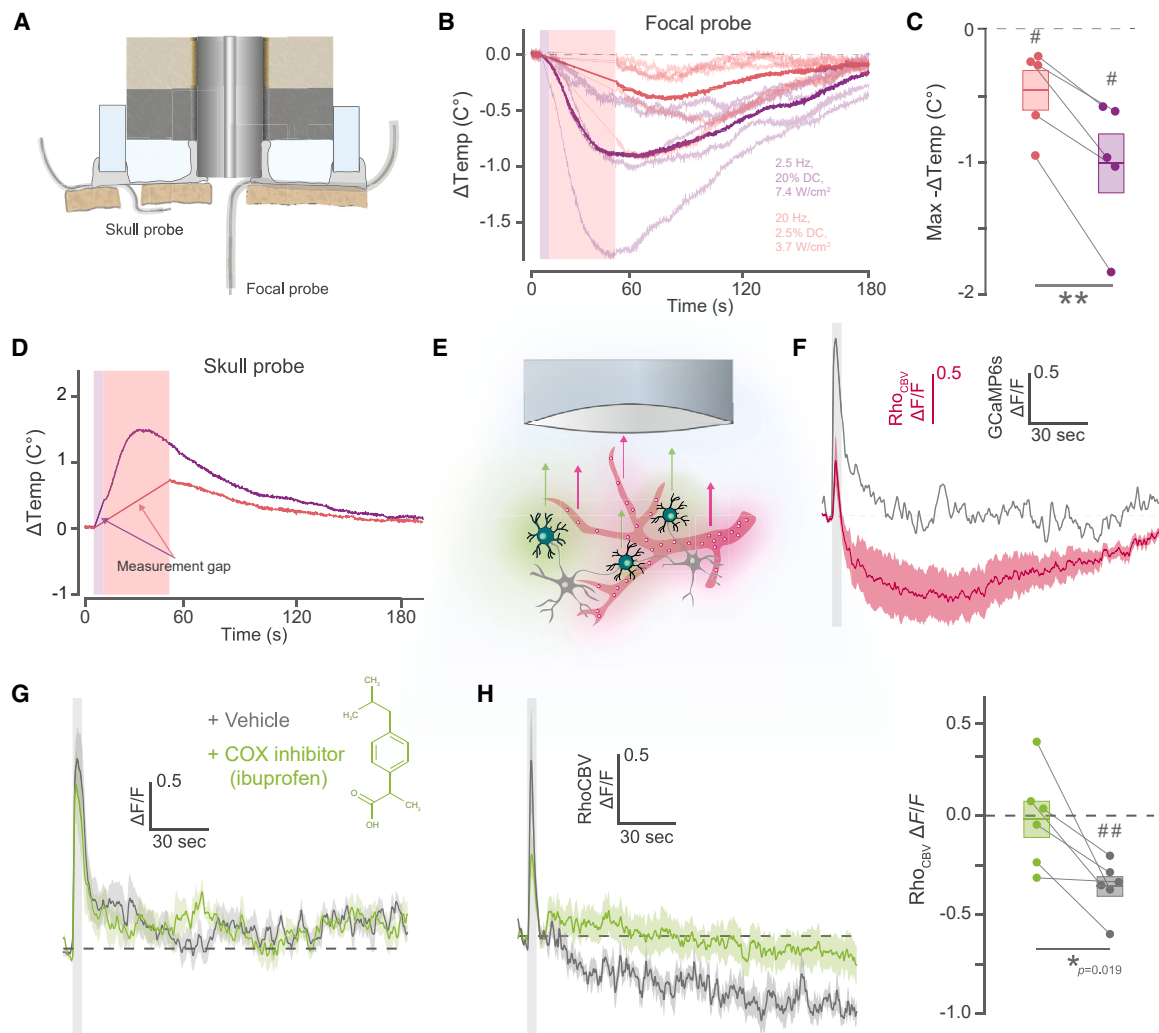


**Figure 5. FUS induces cyclooxygenase-dependent vasoconstriction and deep-brain cooling**

(A) Illustration of a thermocouple probe implanted in place of the optical fiber within the PhoCUS apparatus.

(B and C) Time series of change in focal brain temperature relative to CMT-targeted FUS stimulation (B; line and shaded area represent mean  $\pm$  SEM) and comparison of the maximum decrease in temperature within animals (C;  $n = 5$  animals, bars represent mean  $\pm$  SEM, and circles represent animals for all plots, one-sample t test;  $\#p < 0.05$ , paired two-tailed t test;  $^{**}p < 0.01$ ).

(D) Average traces of thermal recording from skull probe.

(E) Illustration of rhodamine B dextran fluorescence monitored in blood with spectrally separate measurement of GCaMP6s with a time series average of recordings from the CMT.

(F) Time series averages of neural activity (gray) and blood fluorescence (red) relative to FUS stimulus.

(G and H) Time series averages of neural activity (G) and blood volume at the CMT with and without COX inhibitor or saline vehicle administration prior to FUS stimulation with individual change across post stimulus period (H; paired two-tailed t test;  $*p = 0.019$ , one-sample t test;  $^{##}p < 0.01$ ).

injected rhodamine B dextran into the animal's bloodstream and used the non-overlapping optical spectra to simultaneously measure neuronal calcium with GCaMP6s (Figure 5E). As expected, we found a rapid increase in CAMKII+ CMT neuronal activity correlated with a rapid rise in blood volume (Figures 5F, 5G, and S7), consistent with neurovascular coupling observed with other imaging modalities.<sup>71</sup> However, following the initial spike in blood volume, we observed a sustained decrease in volume over the 3-min interstimulus period (Figure 5G). Cyclooxygenase 1 and 2 (COX1/2) couple brain activity to vasodynamics bidirec-

tionally.<sup>72</sup> Although normal increases in neural activity promote vasodilation, substantial increases in neural activity can drive delayed and prolonged vasoconstriction.<sup>72,73</sup> To examine this possible link, we examined blood volume and neural activity in the CMT following ibuprofen (30 mg/kg) or saline injection, since ibuprofen is a potent COX1/2 inhibitor.<sup>74</sup> While neural activity showed no apparent change, the decrease in blood volume was eliminated (Figures 5H and S1), suggesting that strong FUS activation can drive long-lasting neurovascular responses through canonical COX1/2 signaling.

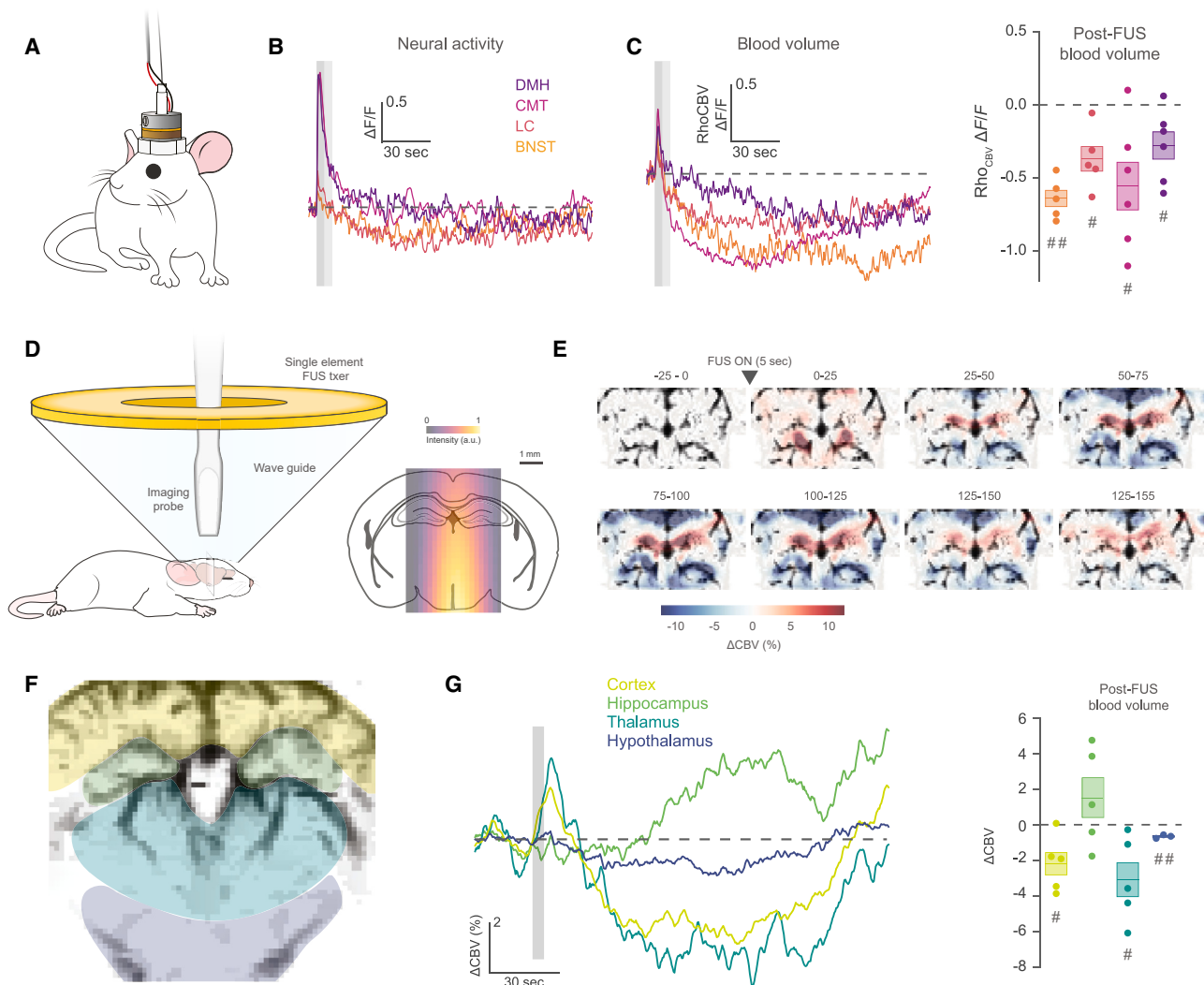


**Figure 6. FUS-induced vasodynamics are brain region dependent**

(A) Illustration of a PhoCUS apparatus for simultaneous recording of brain GCaMP and blood volume.

(B) Time series averages of neural activity for arousal regions during blood fluorescence monitoring.

(C) Time series averages of blood fluorescence for all arousal regions during FUS stimulation with quantification during post-FUS period (15–180 s) (bars represent mean  $\pm$  SEM, and circles represent animals for all plots,  $n = 5$ –6 mice, one-sample t test;  $\#p < 0.05$ , paired two-tailed t test;  $^{**}p < 0.01$ ).

(D) Illustration of system for simultaneous functional ultrasound imaging and stimulation with an intensity overlay.

(E) Representative time series of changes in cerebral blood volume ( $\Delta$ CBV) relative to a 5 s FUS stimulation (2.5 Hz, 5 s, 20% D.C., 18.9 W/cm $^2$ ).

(F and G) Example 2D brain segmentation for quantification (F; hypothalamus visible in 3 of 5 experiments) time series averages of  $\Delta$ CBV across different brain areas during FUS stimulation with quantification during post-FUS period (G; 30–180 s) (bars represent mean  $\pm$  SEM, and circles represent animals for all plots,  $n = 3$ –5 mice, one-sample t test;  $\#p < 0.05$ ,  $^{##}p < 0.01$ ).

To examine whether this phenomenon was related to differences in observed neural activity that varied across brain areas, we measured blood volume following optimized stimulation (2.5 Hz, 10 s, 10% D.C.) of the DMH, LC, and BNST. All three regions showed significant vasoconstriction following the stimuli despite the lesser activation observed in the LC and BNST (Figures 6A–6C). Like the CMT, all regions also maintained a correlation of vasodilation with neural activity during the FUS stimuli (Figure S7A). Intriguingly, increased neural activity did not cause larger post-stimuli vasoconstriction for any region. In fact, larger neural activity was associated with modest vasodilation for the

CMT (Figure S7B). This disassociation suggested that vasoconstriction is likely driven by FUS effects extending beyond local neural activity. To examine the spatial breadth of these effects, we combined ultrafast power-doppler imaging with FUS stimulation to measure cerebral blood volume changes across the focal plane in anesthetized mice (Figures 6D and 6E).<sup>75–78</sup> The optimized stimulus pulsing (2.5 Hz, 5 s, 20% D.C.) was targeted to the CMT using a similar fundamental frequency (500 kHz), intensity (18.9 W/cm $^2$ ), and focal area (Figure 6D). We found that significant vasoconstriction occurred broadly across the thalamus, hypothalamus, and cortex (Figures 6E–6G). Intriguingly, the

hippocampus was resilient against vasoconstriction, suggesting that vasodynamic response propagates beyond the ultrasound focus in a brain-region-dependent manner.

Despite the large changes in neural activity, behavior, and even vascular responses, we did not observe changes in blood corticosterone levels (Figure S8A)<sup>79</sup> or peripheral immune responses (Figures S8B–S8J) following repeated DMH stimulation (10 stimulations, 3-min interval). Thus, behavioral and neurovascular effects were due to neuromodulation rather than non-specific consequences of FUS stimulation and supports the safety of repeated FUS brain stimulation to deep-brain targets, including the hypothalamus.

## DISCUSSION

Here, we examined a wide array of ultrasound pulsing parameters and optimal parameters for both excitation and inhibition across various cell types. Even subtle changes in these parameters resulted in large differences in neuronal activity and ultrasound-induced behavioral outcomes. In examining the impact of PRF on neuromodulation, we discovered clear and bidirectional differences within a narrow frequency bands. In contrast to other brain stimulation techniques and the range chosen here, FUS is often employed with PRFs exceeding the natural spiking rate of neurons. However, higher PRFs increase the audibility of sound and may confound behavioral readouts.<sup>80,81</sup> Thus, we chose to examine a range better aligned with naturalistic firing frequencies. We found that PRF is inversely related to excitation, with lower frequencies having stronger excitation. This finding is well aligned with previous studies that demonstrate that the duration of a single pulse is directly correlated with increased neural activity within a sub-kilohertz frequency regime.<sup>28,30,82</sup> When examining FUS intensity, we found that stimulus-locked neural activity increased with intensity across all cell types.

From a biomechanical standpoint, longer pulse on-off periods may allow for greater displacement of the membrane, which directly increases neuronal firing in retinal slices.<sup>28</sup> In contrast with excitation, the activity of a subset of the cell types was inhibited specifically with 20 Hz stimulation. A possible explanation is that shorter, more frequent pulses may induce repeated subthreshold depolarization, which can cause neuronal adaptation reflected in endogenous spiking and network connectivity.<sup>83</sup> In contrast, other works have found that PRF in the supra-kilohertz range is directly related to neuronal excitation.<sup>32,33</sup> This may fit the proposed theory if pulsing a high PRF itself has the biomechanical appearance of pulsed continuous wave,<sup>32</sup> particularly if the pulse trains are modulated at a low frequency.<sup>32,33</sup> Furthermore, the inhibitory protocol became ineffective outside a narrow intensity range, suggesting that careful titration may improve FUS-induced neural inhibition.

FUS sensitivity is largely thought to be driven by the combinatorial expression of mechanosensitive channels that are heterogeneously expressed across cell types.<sup>10,30,40,84–86</sup> For the parameter sets examined here, we observed differential effects across cell types, consistent with heterogeneous expression profiles.<sup>87</sup> DMH neurons were strikingly sensitive to FUS, while

BNST neurons were largely non-responsive. The DMH is known to express high levels of TRPV1, a powerful actuator of FUS neuromodulation.<sup>67,68,88,89</sup> Previous works have also provided evidence of direct<sup>8</sup> and indirect activation by FUS through TRPM2 neurons of the preoptic area<sup>67</sup> and hypothalamic neuromodulation-induced hypophagia.<sup>90</sup> Intriguingly, BNST neurons express high levels of Piezo1, which has also been shown to confer FUS sensitivity.<sup>40,91</sup> The striking difference between these cell types suggests that higher-dimensional genetic profiling, rather than single gene expression, may be necessary to predict FUS sensitivity. It's also possible that local network effects may override natural ultrasound sensitivity.<sup>16,34</sup>

Overall, the unpredictability of FUS sensitivity suggests that human research would benefit from preclinical examination of target cell types. However, the strong conservation of parametric trends suggests that, in the absence of information, protocols intended to increase neural activity may benefit from lower-PRF, higher-duty-cycle pulsing over shorter periods, and higher intensities. In contrast, protocols intended to inhibit may benefit from PRFs near 20 Hz, with lower duty cycle and prolonged delivery. Intensities for protocols intended to inhibit may need to be carefully titrated to avoid excitation. In a follow-up study, we found that repetition of the excitatory low-PRF, high-duty-cycle, 5 spulse enhanced arousal effects observed when targeting the CMT.<sup>92</sup> Future studies are needed to examine optimal repetition count and intermittent off period for achieving enduring or enhanced neuromodulatory effects.<sup>92</sup>

While the current study employs viral labeling to examine specific subsets of cells within each region, use of high-density electrode arrays, such as the Neuropixels probe,<sup>93</sup> might employ spike sorting to monitor activity of multiple cell types simultaneously. Furthermore, the axial depth of such an electrode could allow examination of spatial effects along the axial focal profile. However, it is unclear whether the source signal can be maintained during FUS-induced tissue motion and extracellular fluid flow. Beyond cell-type-specific delineation, future studies may also use PhoCUS with angled fiber mounting or acoustic lenses to stimulate and record separate brain areas in an effort to elucidate FUS effects on neural circuits.

Beyond the neuronal effects observed, this work highlights the criticality of pulsing regimes in eliciting salient behavioral outcomes. To date, the simplest validation experiments for establishing FUS neuromodulation involve induction of motor events under anesthesia, such as tail or hindlimb twitch.<sup>10,26,27,40,77,82</sup> However, these behaviors are highly sensitive to anesthesia and auditory confound, making interpretability and reproducibility challenging.<sup>94</sup> Here, we demonstrate robust, rapid, and target-specific motor and postural behaviors in awake behaving mice that are clearly visible to an untrained observer (Videos S1 and S2). Using the open-source hardware and software available for PhoCUS,<sup>16</sup> any laboratory equipped for stereotactic mouse surgeries can easily repeat this experiment for validation of FUS neuromodulation. In addition to inducible walking and SAP, we demonstrate increased or decreased head motion with excitatory or inhibitory stimulation parameters, respectively. This level of control is similar to optogenetic experiments in the CMT, where bidirectional control of arousal state was achieved.<sup>48</sup>

In examining physiological effects of optimized FUS waveforms, we found focal cooling at physiologically relevant levels.<sup>95</sup> To our knowledge, FUS-induced focal cooling in the brain has not yet been reported, likely because ultrasound waves deposit thermal energy and most research efforts simulate, rather than measure, focal temperature. However, any changes in fluid flow may serve to increase the distribution of heat from warmer to cooler areas, such as the deep brain to the cortex. In alignment with our study, there are several lines of evidence that FUS can induce vasoconstriction.<sup>96–98</sup> A previous study found that strong induction of astrocyte calcium leads to sustained vasoconstriction with a similar onset time to the effects observed here.<sup>99</sup> Since it is increasingly evident that astrocytes are more sensitive to FUS than neurons,<sup>10,31</sup> it is possible that the stimulations examined here are also engaging astrocytes and cyclooxygenase signaling.<sup>100</sup> This may explain the breadth of vasoconstriction observed where astrocytes may be responding to even the lower pressure observed beyond the focus. While not explicitly examined in this work, it is possible that cerebrospinal fluid (CSF) flow may at least partly explain the thermal change. CSF flow is known to be inversely related to vascular dilation,<sup>101,102</sup> has been shown to increase with brain-wide FUS administration, and may act as a brain coolant because of its relatively rapid exchange with the mucosal sinuses.<sup>103</sup> Thus, increased CSF flow along the perivascular spaces of cranial blood vessels could result in greater convective cooling following FUS<sup>104</sup> and will be of interest for further investigation. In theory, future therapeutics may leverage induced CSF flow for metabolite clearance<sup>105</sup> or in the prevention of Alzheimer's disease.<sup>106</sup>

Collectively, this work provides a framework for examining and optimizing FUS neuromodulation across brain regions and cell types. In the absence of information, the general parameter features described here may inform the base pulse train protocol design for extended delivery, parametrically diverse or single-parameter studies. Nevertheless, the difference in neural and behavioral response to optimal and suboptimal protocols demonstrates the importance of protocol optimization to enhance and expedite therapeutic breakthroughs in the field.

## STAR★METHODS

Detailed methods are provided in the online version of this paper and include the following:

- KEY RESOURCES TABLE
- RESOURCE AVAILABILITY
  - Lead contact
  - Materials availability
  - Data and code availability
- EXPERIMENTAL MODEL AND SUBJECT DETAILS
- METHOD DETAILS
  - Histological imaging
  - Focused ultrasound parameter examination
  - Fiber photometry data collection and analysis
  - Brain temperature monitoring
  - Peripheral auditory brainstem response prediction
  - Audible tone response
  - Optical excitation and inhibition
  - Motion, stretch attend posture, and body temperature quantification
  - Rotarod task

- Blood volume quantification
- Ultrafast power Doppler imaging
- Corticosterone ELISA
- Single-cell mass cytometry

## ● QUANTIFICATION AND STATISTICAL ANALYSIS

## SUPPLEMENTAL INFORMATION

Supplemental information can be found online at <https://doi.org/10.1016/j.neuron.2024.07.002>.

## ACKNOWLEDGMENTS

This work was supported in part by grants from NIH (MH116470 and DA055056 to L.d.L.). K.R.M. was supported by the Ruth L. Kirschstein Postdoctoral Individual National Research Service Award (1F32HL149458-01A1) and the Multi-Institutional Training in Genetic/Genomic Approaches to Sleep Disorders Award (5T32HL110952-08). J.S.F. was supported by a K99 from NINDS (K99NS126725). Relevant work in the laboratory of I.S. was supported by the NIH (NS121106) and the Lennox-Gastaut Syndrome (LGS) Foundation. Functional ultrasound imaging work was funded by NIH grant R01EB027576 to E.E.K. and the German Research Foundation to J.B. We thank Ronald Watkins and Ningrui Li for support in hydrophone scan tank measurements and equipment operation. We thank Dr. Maisie Lo and Dr. Karl Deisseroth for their early guidance provided during the Deisseroth lab fiber photometry workshop.

## AUTHOR CONTRIBUTIONS

Methodology, K.R.M., J.S.F., J.B., A.M., C.L., I.A.S., H.Y., C.C.A., M.C., W.B., T.D., E.M.P., N.M., R.A., B.G., E.K., K.B.P., I.S., and L.d.L.; writing and conceptualization, all authors; investigation, K.R.M., J.S.F., A.M., C.L., I.A.S., H.Y., C.C.A., M.C., W.B., N.L., E.M.P., and N.M.; visualization, K.R.M., I.S., M.C., C.C.A., and E.M.P.; funding acquisition, K.R.M. and L.d.L.

## DECLARATION OF INTERESTS

K.R.M. and L.d.L. are co-inventors on a patent application assigned to Stanford University containing disclosures related to technology used in this article.

Received: November 27, 2023

Revised: May 9, 2024

Accepted: July 2, 2024

Published: July 29, 2024

## REFERENCES

1. Darmani, G., Bergmann, T.O., Butts Pauly, K., Caskey, C.F., de Lecea, L., Fomenko, A., Fouragnan, E., Legon, W., Murphy, K.R., Nandi, T., et al. (2021). Non-invasive transcranial ultrasound stimulation for neuromodulation. *Clin. Neurophysiol.* 135, 51–73. <https://doi.org/10.1016/j.clinph.2021.12.010>.
2. Blackmore, D.G., Razansky, D., and Götz, J. (2023). Ultrasound as a versatile tool for short- and long-term improvement and monitoring of brain function. *Neuron* 111, 1174–1190. <https://doi.org/10.1016/j.neuron.2023.02.018>.
3. Priestley, L., Chiew, M., Shahdloo, M., Mahmoodi, A., Cheng, X., Cleveland, R., Rushworth, M., and Khalighinejad, N. (2024). Dorsal raphe nucleus controls motivational state transitions in monkeys. Preprint at bioRxiv. <https://doi.org/10.1101/2024.02.13.580224>.
4. Folloni, D., Verhagen, L., Mars, R.B., Fouragnan, E., Constans, C., Aubry, J.F., Rushworth, M.F.S., and Sallet, J. (2019). Manipulation of Subcortical and Deep Cortical Activity in the Primate Brain Using Transcranial Focused Ultrasound Stimulation. *Neuron* 101, 1109–1116.e5. <https://doi.org/10.1016/j.neuron.2019.01.019>.
5. Fouragnan, E.F., Chau, B.K.H., Folloni, D., Kolling, N., Verhagen, L., Klein-Flügge, M., Tankelevitch, L., Papageorgiou, G.K., Aubry, J.F.,

- Sallet, J., and Rushworth, M.F.S. (2019). The macaque anterior cingulate cortex translates counterfactual choice value into actual behavioral change. *Nat. Neurosci.* 22, 797–808. <https://doi.org/10.1038/s41593-019-0375-6>.
6. Bubrick, E.J., McDannold, N.J., and White, P.J. (2022). Low Intensity Focused Ultrasound for Epilepsy— A New Approach to Neuromodulation. *Epilepsy Curr.* 22, 156–160. <https://doi.org/10.1177/15357597221086111>.
  7. Verhagen, L., Gallea, C., Folloni, D., Constans, C., Jensen, D.E.A., Ahnline, H., Roumazeilles, L., Santin, M., Ahmed, B., Lehericy, S., et al. (2019). Offline impact of transcranial focused ultrasound on cortical activation in primates. *eLife* 8, e40541. <https://doi.org/10.7554/eLife.40541>.
  8. Pang, N., Meng, W., Zhong, Y., Liu, X., Lin, Z., Guo, T., Zhou, H., Qi, L., Meng, L., Xu, L., and Niu, L. (2022). Ultrasound Deep Brain Stimulation Modulates Body Temperature in Mice. *IEEE Trans. Neural Syst. Rehabil. Eng.* 30, 1851–1857. <https://doi.org/10.1109/TNSRE.2022.3188516>.
  9. Chu, P.C., Huang, C.S., Ing, S.Z., Yu, H.Y., Fisher, R.S., and Liu, H.L. (2023). Pulsed Focused Ultrasound Reduces Hippocampal Volume Loss and Improves Behavioral Performance in the Kainic Acid Rat Model of Epilepsy. *Neurotherapeutics* 20, 502–517. <https://doi.org/10.1007/s13311-023-01363-7>.
  10. Oh, S.J., Lee, J.M., Kim, H.B., Lee, J., Han, S., Bae, J.Y., Hong, G.S., Koh, W., Kwon, J., Hwang, E.S., et al. (2019). Ultrasonic Neuromodulation via Astrocytic TRPA1. *Curr. Biol.* 29, 3386–3401.e8. <https://doi.org/10.1016/j.cub.2019.08.021>.
  11. Lin, W.T., Chen, R.C., Lu, W.W., Liu, S.H., and Yang, F.Y. (2015). Protective effects of low-intensity pulsed ultrasound on aluminum-induced cerebral damage in Alzheimer's disease rat model. *Sci. Rep.* 5, 9671–9677. <https://doi.org/10.1038/srep09671>.
  12. Leinenga, G., and Götz, J. (2015). Scanning ultrasound removes amyloid- $\beta$  and restores memory in an Alzheimer's disease mouse model. *Sci. Transl. Med.* 7, 278ra33. <https://doi.org/10.1126/scitranslmed.aaa2512>.
  13. Bobola, M.S., Chen, L., Ezeokeke, C.K., Olmstead, T.A., Nguyen, C., Sahota, A., Williams, R.G., and Mourad, P.D. (2020). Transcranial focused ultrasound, pulsed at 40 Hz, activates microglia acutely and reduces  $\text{A}\beta$  load chronically, as demonstrated in vivo. *Brain Stimul.* 13, 1014–1023. <https://doi.org/10.1016/j.brs.2020.03.016>.
  14. Baek, H., Pahk, K.J., Kim, M.-J., Youn, I., and Kim, H. (2018). Modulation of cerebellar cortical plasticity using low-intensity focused ultrasound for poststroke sensorimotor function recovery. *Neurorehabil. Neural Repair* 32, 777–787. <https://doi.org/10.1177/1545968318790022>.
  15. Hakimova, H., Kim, S., Chu, K., Lee, S.K., Jeong, B., and Jeon, D. (2015). Ultrasound stimulation inhibits recurrent seizures and improves behavioral outcome in an experimental model of mesial temporal lobe epilepsy. *Epilepsy Behav.* 49, 26–32. <https://doi.org/10.1016/j.yebeh.2015.04.008>.
  16. Murphy, K.R., Farrell, J.S., Gomez, J.L., Stedman, Q.G., Li, N., Leung, S.A., Good, C.H., Qiu, Z., Firouzi, K., Pauly, K.B., et al. (2022). A tool for monitoring cell type-specific focused ultrasound neuromodulation and control of chronic epilepsy. *Proc. Natl. Acad. Sci. USA* 119, e2206828119. <https://doi.org/10.1073/pnas.2206828119>.
  17. Li, X., Yang, H., Yan, J., Wang, X., and Yuan, Y. (2019). Low-intensity pulsed ultrasound stimulation modulates the nonlinear dynamics of local field potentials in temporal lobe epilepsy. *Front. Neurosci.* 13, 287. <https://doi.org/10.3389/fnins.2019.00287>.
  18. Velling, V.A., and Shklyaruk, S.P. (1988). Modulation of the functional state of the brain with the aid of focused ultrasonic action. *Neurosci. Behav. Physiol.* 18, 369–375. <https://doi.org/10.1007/BF01193880>.
  19. Webb, T.D., Wilson, M.G., Odéen, H., and Kubanek, J. (2023). Sustained modulation of primate deep brain circuits with focused ultrasonic waves. *Brain Stimul.* 16, 798–805. <https://doi.org/10.1016/j.brs.2023.04.012>.
  20. Bian, T., Meng, W., Qiu, M., Zhong, Z., Lin, Z., Zou, J., Wang, Y., Huang, X., Xu, L., Yuan, T., et al. (2021). Noninvasive Ultrasound Stimulation of Ventral Tegmental Area Induces Reanimation from General Anaesthesia in Mice. *Research* 2021, 2674692. <https://doi.org/10.34133/2021/2674692>.
  21. Kubanek, J., Brown, J., Ye, P., Pauly, K.B., Moore, T., and Newsome, W. (2020). Remote, brain region-specific control of choice behavior with ultrasonic waves. *Sci. Adv.* 6, eaaz4193. <https://doi.org/10.1126/sciadv.aaz4193>.
  22. Niu, X., Yu, K., and He, B. (2022). Transcranial focused ultrasound induces sustained synaptic plasticity in rat hippocampus. *Brain Stimul.* 15, 352–359. <https://doi.org/10.1016/j.brs.2022.01.015>.
  23. Strohman, A., Payne, B., In, A., Stebbins, K., and Legon, W. (2024). Low-Intensity Focused Ultrasound to the Human Dorsal Anterior Cingulate Attenuates Acute Pain Perception and Autonomic Responses. *J. Neurosci.* 44, e1011232023. <https://doi.org/10.1523/JNEUROSCI.1011-23.2023>.
  24. Zeng, K., Darmani, G., Fomenko, A., Xia, X., Tran, S., Nankoo, J.-F., Shamli Oghli, Y., Wang, Y., Lozano, A., and Chen, R. (2021). Induction of human motor cortex plasticity by theta burst transcranial ultrasound stimulation. *Brain Stimul.* 14, 1592. <https://doi.org/10.1016/j.brs.2021.10.013>.
  25. Munoz, F., Meaney, A., Gross, A., Liu, K., Pouliopoulos, A.N., Liu, D., Konofagou, E.E., and Ferrera, V.P. (2022). Long term study of motivational and cognitive effects of low-intensity focused ultrasound neuromodulation in the dorsal striatum of nonhuman primates. *Brain Stimul.* 15, 360–372. <https://doi.org/10.1016/j.brs.2022.01.014>.
  26. King, R.L., Brown, J.R., Newsome, W.T., and Pauly, K.B. (2013). Effective parameters for ultrasound-induced in vivo neurostimulation. *Ultrasound Med. Biol.* 39, 312–331. <https://doi.org/10.1016/j.ultrasmedbio.2012.09.009>.
  27. Ye, P.P., Brown, J.R., and Pauly, K.B. (2016). Frequency dependence of ultrasound neurostimulation in the mouse brain. *Ultrasound Med. Biol.* 42, 1512–1530. <https://doi.org/10.1016/j.ultrasmedbio.2016.02.012>.
  28. Menz, M.D., Ye, P., Firouzi, K., Nikoozadeh, A., Pauly, K.B., Khuri-Yakub, P., and Baccus, S.A. (2019). Radiation Force as a Physical Mechanism for Ultrasonic Neurostimulation of the Ex Vivo Retina. *J. Neurosci.* 39, 6251–6264. <https://doi.org/10.1523/JNEUROSCI.2394-18.2019>.
  29. Kubanek, J., Shukla, P., Das, A., Baccus, S.A., and Goodman, M.B. (2018). Ultrasound elicits behavioral responses through mechanical effects on neurons and ion channels in a simple nervous system. *J. Neurosci.* 38, 3081–3091. <https://doi.org/10.1523/JNEUROSCI.1458-17.2018>.
  30. Yoo, S., Mittelstein, D.R., Hurt, R.C., Lacroix, J., and Shapiro, M.G. (2022). Focused ultrasound excites cortical neurons via mechanosensitive calcium accumulation and ion channel amplification. *Nat. Commun.* 13, 493. <https://doi.org/10.1038/s41467-022-28040-1>.
  31. Lee, K., Lee, J.M., Phan, T.T., Lee, C.J., Park, J.M., and Park, J. (2023). Ultrasoundcoverslip: In-vitro platform for high-throughput assay of cell type-specific neuromodulation with ultra-low-intensity ultrasound stimulation. *Brain Stimul.* 16, 1533–1548. <https://doi.org/10.1016/j.brs.2023.08.002>.
  32. Yu, K., Niu, X., Krook-Magnuson, E., and He, B. (2021). Intrinsic functional neuron-type selectivity of transcranial focused ultrasound neuro-modulation. *Nat. Commun.* 12, 2519. <https://doi.org/10.1038/s41467-021-22743-7>.
  33. Manuel, T.J., Kusunose, J., Zhan, X., Lv, X., Kang, E., Yang, A., Xiang, Z., and Caskey, C.F. (2020). Ultrasound neuromodulation depends on pulse repetition frequency and can modulate inhibitory effects of TTX. *Sci. Rep.* 10, 15347. <https://doi.org/10.1038/s41598-020-72189-y>.
  34. Murphy, K.R., and de Lecea, L. (2023). Cell type specific focused ultrasound neuromodulation in preclinical models of sleep and psychiatric disorders. *Neuropharmacology* 49, 299–300. <https://doi.org/10.1038/s41386-023-01662-9>.

35. Young, R.R., and Henneman, E. (1961). Functional effects of focused ultrasound on mammalian nerves. *Science* 134, 1521–1522. <https://doi.org/10.1126/science.134.3489.1521>.
36. Hoffman, B.U., Baba, Y., Lee, S.A., Tong, C.K., Konofagou, E.E., and Lumpkin, E.A. (2022). Focused ultrasound excites action potentials in mammalian peripheral neurons in part through the mechanically gated ion channel PIEZO2. *Proc. Natl. Acad. Sci. USA* 119, e2115821119. <https://doi.org/10.1073/pnas.2115821119>.
37. Yaakub, S.N., White, T.A., Roberts, J., Martin, E., Verhagen, L., Stagg, C.J., Hall, S., and Fouragnan, E.F. (2023). Transcranial focused ultrasound-mediated neurochemical and functional connectivity changes in deep cortical regions in humans. *Nat. Commun.* 14, 5318. <https://doi.org/10.1038/s41467-023-40998-0>.
38. Yang, P.F., Phipps, M.A., Jonathan, S., Newton, A.T., Byun, N., Gore, J.C., Grissom, W.A., Caskey, C.F., and Chen, L.M. (2021). Bidirectional and state-dependent modulation of brain activity by transcranial focused ultrasound in non-human primates. *Brain Stimul.* 14, 261–272. <https://doi.org/10.1016/j.brs.2021.01.006>.
39. Park, M., Hoang, G.M., Nguyen, T., Lee, E., Jung, H.J., Choe, Y., Lee, M.H., Hwang, J.Y., Kim, J.G., and Kim, T. (2021). Effects of transcranial ultrasound stimulation pulsed at 40 Hz on A $\beta$  plaques and brain rhythms in 5 $\times$ FAD mice. *Transl. Neurodegener.* 10, 48. <https://doi.org/10.1186/s40035-021-00274-x>.
40. Zhu, J., Xian, Q., Hou, X., Wong, K.F., Zhu, T., Chen, Z., He, D., Kala, S., Murugappan, S., Jing, J., et al. (2023). The mechanosensitive ion channel Piezo1 contributes to ultrasound neuromodulation. *Proc. Natl. Acad. Sci. USA* 120, e2300291120. <https://doi.org/10.1073/pnas.2300291120>.
41. Adamantidis, A.R., Zhang, F., Aravanis, A.M., Deisseroth, K., and De Lecea, L. (2007). Neural substrates of awakening probed with optogenetic control of hypocretin neurons. *Nature* 450, 420–424. <https://doi.org/10.1038/nature06310>.
42. Kuncel, A.M., and Grill, W.M. (2004). Selection of stimulus parameters for deep brain stimulation. *Clin. Neurophysiol.* 115, 2431–2441. <https://doi.org/10.1016/j.clinph.2004.05.031>.
43. Carter, M.E., Yizhar, O., Chikahisa, S., Nguyen, H., Adamantidis, A., Nishino, S., Deisseroth, K., and De Lecea, L. (2010). Tuning arousal with optogenetic modulation of locus coeruleus neurons. *Nat. Neurosci.* 13, 1526–1533. <https://doi.org/10.1038/nn.2682>.
44. Cardin, J.A., Carlén, M., Meletis, K., Knoblich, U., Zhang, F., Deisseroth, K., Tsai, L.H., and Moore, C.I. (2009). Driving fast-spiking cells induces gamma rhythm and controls sensory responses. *Nature* 459, 663–667. <https://doi.org/10.1038/nature08002>.
45. Rubens, M.T., and Zanto, T.P. (2012). Parameterization of transcranial magnetic stimulation. *J. Neurophysiol.* 107, 1257–1259. <https://doi.org/10.1152/jn.00716.2011>.
46. Darrow, D.P., O'Brien, P., Richner, T.J., Netoff, T.I., and Ebbini, E.S. (2019). Reversible neuroinhibition by focused ultrasound is mediated by a thermal mechanism. *Brain Stimul.* 12, 1439–1447. <https://doi.org/10.1016/j.brs.2019.07.015>.
47. Wright, S.J. (2015). Coordinate descent algorithms. *Math. Program.* 151, 3–34. <https://doi.org/10.1007/s10107-015-0892-3>.
48. Gent, T.C., Bandarabadi, M., Herrera, C.G., and Adamantidis, A.R. (2018). Thalamic dual control of sleep and wakefulness. *Nat. Neurosci.* 21, 974–984. <https://doi.org/10.1038/s41593-018-0164-7>.
49. Baker, R., Gent, T.C., Yang, Q., Parker, S., Vyssotski, A.L., Wisden, W., Brickley, S.G., and Franks, N.P. (2014). Altered activity in the central medial thalamus precedes changes in the neocortex during transitions into both sleep and propofol anesthesia. *J. Neurosci.* 34, 13326–13335. <https://doi.org/10.1523/JNEUROSCI.1519-14.2014>.
50. Velasco, A.L., Velasco, F., Jiménez, F., Velasco, M., Castro, G., Carrillo-Ruiz, J.D., Fanghanel, G., and Boleaga, B. (2006). Neuromodulation of the centromedian thalamic nuclei in the treatment of generalized seizures and the improvement of the quality of life in patients with Lennox-Gastaut syndrome. *Epilepsia* 47, 1203–1212. <https://doi.org/10.1111/j.1528-1167.2006.00593.x>.
51. Kamimura, H.A.S., Wang, S., Chen, H., Wang, Q., Aurup, C., Acosta, C., Carneiro, A.A.O., and Konofagou, E.E. (2016). Focused ultrasound neuromodulation of cortical and subcortical brain structures using 1.9 MHz. *Med. Phys.* 43, 5730. <https://doi.org/10.1118/1.4963208>.
52. Cain, J.A., Spivak, N.M., Coetzee, J.P., Crone, J.S., Johnson, M.A., Lutkenhoff, E.S., Real, C., Buitrago-Blanco, M., Vespa, P.M., Schnakers, C., and Monti, M.M. (2022). Ultrasonic Deep Brain Neuromodulation in Acute Disorders of Consciousness: A Proof-of-Concept. *Brain Sci.* 12, 428. <https://doi.org/10.3390/brainsci12040428>.
53. Otgon-Uul, Z., Suyama, S., Onodera, H., and Yada, T. (2016). Optogenetic activation of leptin- and glucose-regulated GABAergic neurons in dorsomedial hypothalamus promotes food intake via inhibitory synaptic transmission to paraventricular nucleus of hypothalamus. *Mol. Metab.* 5, 709–715. <https://doi.org/10.1016/j.molmet.2016.06.010>.
54. Li, D.P., Zhou, J.J., Zhang, J., and Pan, H.L. (2017). CaMKII regulates synaptic NMDA receptor activity of hypothalamic presynaptic neurons and sympathetic outflow in hypertension. *J. Neurosci.* 37, 10690–10699. <https://doi.org/10.1523/JNEUROSCI.2141-17.2017>.
55. Helfferich, F., and Palkovits, M. (2003). Acute audiogenic stress-induced activation of CRH neurons in the hypothalamic paraventricular nucleus and catecholaminergic neurons in the medulla oblongata. *Brain Res.* 975, 1–9. [https://doi.org/10.1016/S0006-8993\(03\)02509-5](https://doi.org/10.1016/S0006-8993(03)02509-5).
56. Sato, T., Shapiro, M.G., and Tsao, D.Y. (2018). Ultrasonic Neuromodulation Causes Widespread Cortical Activation via an Indirect Auditory Mechanism. *Neuron* 98, 1031–1041.e5. <https://doi.org/10.1016/j.neuron.2018.05.009>.
57. Guo, H., Hamilton, M., Offutt, S.J., Gloeckner, C.D., Li, T., Kim, Y., Legon, W., Alford, J.K., and Lim, H.H. (2018). Ultrasound Produces Extensive Brain Activation via a Cochlear Pathway. *Neuron* 98, 1020–1030.e4. <https://doi.org/10.1016/j.neuron.2018.04.036>.
58. Johnstone, A., Nandi, T., Martin, E., Bestmann, S., Stagg, C., and Treeby, B. (2021). A range of pulses commonly used for human transcranial ultrasound stimulation are clearly audible. *Brain Stimul.* 14, 1353–1355. <https://doi.org/10.1016/j.brs.2021.08.015>.
59. Choi, M.H., Li, N., Popelka, G., and Pauly, K.B. (2023). Development and validation of a computational method to predict unintended auditory brainstem response during transcranial ultrasound neuromodulation in mice. *Brain Stimul.* 16, 1362–1370. <https://doi.org/10.1016/j.brs.2023.01.001>.
60. Salahshoor, H., Shapiro, M.G., and Ortiz, M. (2020). Transcranial focused ultrasound generates skull-conducted shear waves: Computational model and implications for neuromodulation. *Appl. Phys. Lett.* 117, 033702. <https://doi.org/10.1063/5.0011837>.
61. Wang, Y., Song, Y., Tong, L., Wang, L., Cao, J., Qin, G., Liu, X., Mi, W., Wang, E., and Guo, Y. (2023). GABAergic neurons in the dorsomedial hypothalamus regulate states of consciousness in sevoflurane anesthesia. *iScience* 26, 105913. <https://doi.org/10.1016/j.isci.2022.105913>.
62. Jardim, M.C., and Guimarães, F.S. (2004). Role of glutamate ionotropic receptors in the dorsomedial hypothalamic nucleus on anxiety and locomotor behavior. *Pharmacol. Biochem. Behav.* 79, 541–546. <https://doi.org/10.1016/j.pbb.2004.09.005>.
63. Gooley, J.J., Schomer, A., and Saper, C.B. (2006). The dorsomedial hypothalamic nucleus is critical for the expression of food-entrainable circadian rhythms. *Nat. Neurosci.* 9, 398–407. <https://doi.org/10.1038/nn1651>.
64. Holly, K.S., Orndorff, C.O., and Murray, T.A. (2016). MATSAP: An automated analysis of stretch-Attend posture in rodent behavioral experiments. *Sci. Rep.* 6, 31286. <https://doi.org/10.1038/srep31286>.
65. Zahler, S.H., Taylor, D.E., Wong, J.Y., Adams, J.M., and Feinberg, E.H. (2021). Superior colliculus drives stimulus-evoked directionally biased saccades and attempted head movements in head-fixed mice. *eLife* 10, e73081. <https://doi.org/10.7554/eLife.73081>.

66. James, M.H., Campbell, E.J., and Dayas, C.V. (2017). Role of the Orexin/Hypocretin system in stress-related psychiatric disorders. *Curr. Top. Behav. Neurosci.* 33, 197–219. [https://doi.org/10.1007/7854\\_2016\\_56](https://doi.org/10.1007/7854_2016_56).
67. Yang, Y., Yuan, J., Field, R.L., Ye, D., Hu, Z., Xu, K., Xu, L., Gong, Y., Yue, Y., Kravitz, A.V., et al. (2023). Induction of a torpor-like hypothermic and hypometabolic state in rodents by ultrasound. *Nat. Metab.* 5, 789–803.
68. Darlow, D.P. (2019). Focused Ultrasound for Neuromodulation. *Neurotherapeutics* 16, 88–99. <https://doi.org/10.1007/s13311-018-00691-3>.
69. Leung, S.A., Webb, T.D., Bitton, R.R., Ghanouni, P., and Butts Pauly, K. (2019). A rapid beam simulation framework for transcranial focused ultrasound. *Sci. Rep.* 9, 7965. <https://doi.org/10.1038/s41598-019-43775-6>.
70. Pasquinelli, C., Hanson, L.G., Siebner, H.R., Lee, H.J., and Thielscher, A. (2019). Safety of transcranial focused ultrasound stimulation: A systematic review of the state of knowledge from both human and animal studies. *Brain Stimul.* 12, 1367–1380. <https://doi.org/10.1016/j.brs.2019.07.024>.
71. Nunez-Elizalde, A.O., Krumin, M., Reddy, C.B., Montaldo, G., Urban, A., Harris, K.D., and Carandini, M. (2022). Neural correlates of blood flow measured by ultrasound. *Neuron* 110, 1631–1640.e4. <https://doi.org/10.1016/j.neuron.2022.02.012>.
72. Mitchell, J.A., Shala, F., Pires, M.E.L., Loy, R.Y., Ravendren, A., Benson, J., Urquhart, P., Nicolaou, A., Herschman, H.R., and Kirkby, N.S. (2021). Endothelial cyclooxygenase-1 paradoxically drives local vasoconstriction and atherosogenesis despite underpinning prostacyclin generation. *Sci. Adv.* 7, eabf6054. <https://doi.org/10.1126/sciadv.abf6054>.
73. Farrell, J.S., Gaxiola-Valdez, I., Wolff, M.D., David, L.S., Dika, H.I., Geeraert, B.L., Wang, X.R., Singh, S., Spanswick, S.C., Dunn, J.F., et al. (2016). Postictal behavioural impairments are due to a severe prolonged hypoperfusion/hypoxia event that is COX-2 dependent. *eLife* 5, e19352. <https://doi.org/10.7554/eLife.19352>.
74. van Hecken, A., Schwartz, J.I., Depré, M., de Lepeleire, I., Dallob, A., Tanaka, W., Wynants, K., Buntinx, A., Arnout, J., Wong, P.H., et al. (2000). Comparative Inhibitory Activity of Rofecoxib, Meloxicam, Diclofenac, Ibuprofen, and Naproxen on COX-2 versus COX-1 in Healthy Volunteers. *J. Clin. Pharmacol.* 40, 1109–1120. <https://doi.org/10.1177/00912700004001005>.
75. Aurup, C., Bendig, J., Blackman, S.G., McCune, E.P., Bae, S., Jimenez-Gambin, S., Ji, R., and Konofagou, E.E. (2024). Transcranial Functional Ultrasound Imaging Detects Focused Ultrasound Neuromodulation Induced Hemodynamic Changes in Mouse and Nonhuman Primate Brains *In Vivo*. Preprint at bioRxiv. <https://doi.org/10.1101/2024.03.08.583971>.
76. Kim, S., Kwon, N., Hossain, M.M., Bendig, J., and Konofagou, E.E. (2024). Functional ultrasound (fUS) imaging of displacement-guided focused ultrasound (FUS) neuromodulation in mice. Preprint at bioRxiv. <https://doi.org/10.1101/2024.03.29.587355>.
77. Aurup, C., Kamimura, H.A.S., and Konofagou, E.E. (2021). High-Resolution Focused Ultrasound Neuromodulation Induces Limb-Specific Motor Responses in Mice *In Vivo*. *Ultrasound Med. Biol.* 47, 998–1013. <https://doi.org/10.1016/j.ultrasmedbio.2020.12.013>.
78. Aurup, C., Pouliopoulos, A.N., Kwon, N., Murillo, M.F., and Konofagou, E.E. (2023). Evaluation of Non-invasive Optogenetic Stimulation with Transcranial Functional Ultrasound Imaging. *Ultrasound Med. Biol.* 49, 908–917. <https://doi.org/10.1016/j.ultrasmedbio.2022.11.002>.
79. Albrechet-Souza, L., Cristina de Carvalho, M., Rodrigues Franci, C., and Brandão, M.L. (2007). Increases in plasma corticosterone and stretched-attend postures in rats naive and previously exposed to the elevated plus-maze are sensitive to the anxiolytic-like effects of midazolam. *Horm. Behav.* 52, 267–273. <https://doi.org/10.1016/j.yhbeh.2007.05.002>.
80. Fomenko, A., Chen, K.H.S., Nankoo, J.F., Saravanamuttu, J., Wang, Y., El-Baba, M., Xia, X., Seeralu, S.S., Hyynnen, K., Lozano, A.M., and Chen, R. (2020). Systematic examination of low-intensity ultrasound parameters on human motor cortex excitability and behavior. *eLife* 9, e54497. <https://doi.org/10.7554/eLife.54497>.
81. Kop, B.R., Shamli Oghli, Y., Grippo, T.C., Nandi, T., Lefkes, J., Meijer, S.W., Farboud, S., Engels, M., Hamani, M., Null, M., et al. (2023). Auditory confounds can drive online effects of transcranial ultrasonic stimulation in humans. *eLife* 12, RP88762. <https://doi.org/10.7554/eLife.88762>.
82. Mohammadjavadi, M., Ye, P.P., Xia, A., Brown, J., Popelka, G., and Pauly, K.B. (2019). Elimination of peripheral auditory pathway activation does not affect motor responses from ultrasound neuromodulation. *Brain Stimul.* 12, 901–910. <https://doi.org/10.1016/j.brs.2019.03.005>.
83. Soldado-Magraner, S., Bandalise, F., Honnuraiah, S., Pfeiffer, M., Moulinier, M., Gerber, U., and Douglas, R. (2020). Conditioning by sub-threshold synaptic input changes the intrinsic firing pattern of CA3 hippocampal neurons. *J. Neurophysiol.* 123, 90–106. <https://doi.org/10.1152/jn.00506.2019>.
84. Prieto, M.L., Firouzi, K., Khuri-Yakub, B.T., and Maduke, M. (2018). Activation of Piezo1 but Not NaV1.2 Channels by Ultrasound at 43 MHz. *Ultrasound Med. Biol.* 44, 1217–1232. <https://doi.org/10.1016/j.ultrasmedbio.2017.12.020>.
85. Kubanek, J., Shi, J., Marsh, J., Chen, D., Deng, C., and Cui, J. (2016). Ultrasound modulates ion channel currents. *Sci. Rep.* 6, 24170. <https://doi.org/10.1038/srep24170>.
86. Sorum, B., Rietmeijer, R.A., Gopakumar, K., Adesnik, H., and Brohawn, S.G. (2021). Ultrasound activates mechanosensitive TRAAK K<sup>+</sup> channels through the lipid membrane. *Proc. Natl. Acad. Sci. USA* 118, e2006980118. <https://doi.org/10.1073/pnas.2006980118>.
87. Yao, Z., van Velthoven, C.T.J., Nguyen, T.N., Goldy, J., Sedeno-Cortes, A.E., Baftizadeh, F., Bertagnoli, D., Casper, T., Chiang, M., Crichton, K., et al. (2021). A taxonomy of transcriptomic cell types across the isocortex and hippocampal formation. *Cell* 184, 3222–3241.e26. <https://doi.org/10.1016/j.cell.2021.04.021>.
88. Xu, K., Yang, Y., Hu, Z., Yue, Y., Gong, Y., Cui, J., Culver, J.P., Bruchas, M.R., and Chen, H. (2023). TRPV1-mediated sonogenetic neuromodulation of motor cortex in freely moving mice. *J. Neural. Eng.* 20, 016055. <https://doi.org/10.1088/1741-2552/acbbba0>.
89. Molinas, A.J.R., Desmoulins, L.D., Hamling, B.V., Butcher, S.M., Anwar, I.J., Miyata, K., Enix, C.L., Dugas, C.M., Satou, R., Derbenev, A.V., and Zsombok, A. (2019). Interaction between trpv1-expressing neurons in the hypothalamus. *J. Neurophysiol.* 121, 140–151. <https://doi.org/10.1152/jn.00004.2018>.
90. Meng, W., Lin, Z., Bian, T., Chen, X., Meng, L., Yuan, T., Niu, L., and Zheng, H. (2024). Ultrasound Deep Brain Stimulation Regulates Food Intake and Body Weight in Mice. *IEEE Trans. Neural Syst. Rehabil. Eng.* 32, 366–377. <https://doi.org/10.1109/TNSRE.2024.3351312>.
91. Partridge, J.G., Forcelli, P.A., Luo, R., Cashdan, J.M., Schulkin, J., Valentino, R.J., and Vicini, S. (2016). Stress increases GABAergic neurotransmission in CRF neurons of the central amygdala and bed nucleus stria terminalis. *Neuropharmacology* 107, 239–250. <https://doi.org/10.1016/j.neuropharm.2016.03.029>.
92. Di Ianni, T., Morrison, K.P., Yu, B., Murphy, K.R., de Lecea, L., and Airan, R.D. (2023). High-throughput ultrasound neuromodulation in awake and freely behaving rats. *Brain Stimul.* 16, 1743–1752. <https://doi.org/10.1016/j.brs.2023.11.014>.
93. Jun, J.J., Steinmetz, N.A., Siegle, J.H., Denman, D.J., Bauza, M., Barbarits, B., Lee, A.K., Anastassiou, C.A., Andrei, A., Aydin, C., et al. (2017). Fully integrated silicon probes for high-density recording of neural activity. *Nature* 551, 232–236. <https://doi.org/10.1038/nature24636>.
94. Kamimura, H.A.S., Conti, A., Toschi, N., and Konofagou, E.E. (2020). Ultrasound neuromodulation: Mechanisms and the potential of multimodal stimulation for neuronal function assessment. *Front. Phys.* 8, 150. <https://doi.org/10.3389/fphy.2020.00150>.

95. Petersen, P.C., Voroslakos, M., and Buzsáki, G. (2022). Brain temperature affects quantitative features of hippocampal sharp wave ripples. *J. Neurophysiol.* 127, 1417–1425. <https://doi.org/10.1152/jn.00047.2022>.
96. Döring, K., Schroeder, H., Fischer, A., Sperling, S., Ninkovic, M., Stadelmann, C., Mielke, D., Rohde, V., and Malinova, V. (2022). In Vivo Vasospasm Induction by Ultrasound Application in the Chicken Chorioallantoic Membrane Model. *Transl. Stroke Res* 13, 616–624. <https://doi.org/10.1007/s12975-021-00960-y>.
97. Martin, E.M., Duck, F.A., and Winlove, C.P. (2012). Thermally-Mediated Ultrasound-Induced Contraction of Equine Muscular Arteries In Vitro and an Investigation of the Associated Cellular Mechanisms. *Ultrasound Med. Biol.* 38, 152–161. <https://doi.org/10.1016/j.ultrasmedbio.2011.10.017>.
98. Pichardo, S., Milleret, R., Curiel, L., Pichot, O., and Chapelon, J.Y. (2006). In vitro experimental study on the treatment of superficial venous insufficiency with high-intensity focused ultrasound. *Ultrasound Med. Biol.* 32, 883–891. <https://doi.org/10.1016/j.ultrasmedbio.2006.02.1419>.
99. Tran, C.H.T., George, A.G., Teskey, G.C., and Gordon, G.R. (2020). Seizures elevate gliovascular unit Ca<sup>2+</sup> and cause sustained vasoconstriction. *JCI Insight* 5, e136469. <https://doi.org/10.1172/jci.insight.136469>.
100. Haidey, J.N., Peringod, G., Institoris, A., Gorzo, K.A., Nicola, W., Vandal, M., Ito, K., Liu, S., Fielding, C., Visser, F., et al. (2021). Astrocytes regulate ultra-slow arteriole oscillations via stretch-mediated TRPV4-COX-1 feedback. *Cell Rep.* 36, 109405. <https://doi.org/10.1016/j.celrep.2021.109405>.
101. Fultz, N.E., Bonmassar, G., Setsompop, K., Stickgold, R.A., Rosen, B.R., Polimeni, J.R., and Lewis, L.D. (2019). Coupled electrophysiological, hemodynamic, and cerebrospinal fluid oscillations in human sleep. *Science* 366, 628–631. <https://doi.org/10.1126/science.aax5440>.
102. Mestre, H., Tithof, J., Du, T., Song, W., Peng, W., Sweeney, A.M., Olveda, G., Thomas, J.H., Nedergaard, M., and Kelley, D.H. (2018). Flow of cerebrospinal fluid is driven by arterial pulsations and is reduced in hypertension. *Nat. Commun.* 9, 4878. <https://doi.org/10.1038/s41467-018-07318-3>.
103. Burhan, H., and Cherian, I. (2020). Brain Cooling and Cleaning: A New Perspective in Cerebrospinal Fluid (CSF) Dynamics. In *New Insight into Cerebrovascular Diseases - An Updated Comprehensive Review*, P.B. Ambrosi, R. Ahmad, A. Abdullahi, and A. Agrawal, eds. (IntechOpen). <https://doi.org/10.5772/intechopen.90484>.
104. Pulous, F.E., Cruz-Hernández, J.C., Yang, C., Kaya, Z., Paccalet, A., Wojtkiewicz, G., Capen, D., Brown, D., Wu, J.W., Schloss, M.J., et al. (2022). Cerebrospinal fluid can exit into the skull bone marrow and instruct cranial hematopoiesis in mice with bacterial meningitis. *Nat. Neurosci.* 25, 567–576. <https://doi.org/10.1038/s41593-022-01060-2>.
105. Xie, L., Kang, H., Xu, Q., Chen, M.J., Liao, Y., Thiagarajan, M., O'Donnell, J., Christensen, D.J., Nicholson, C., Iliff, J.J., et al. (2013). Sleep drives metabolite clearance from the adult brain. *Science* 342, 373–377. <https://doi.org/10.1126/science.1241224>.
106. De Leon, M.J., Li, Y., Okamura, N., Tsui, W.H., Saint-Louis, L.A., Glodzik, L., Osorio, R.S., Fortea, J., Butler, T., Pirraglia, E., et al. (2017). Cerebrospinal fluid clearance in Alzheimer disease measured with dynamic PET. *J. Nucl. Med.* 58, 1471–1476. <https://doi.org/10.2967/jnumed.116.187211>.
107. Koay, G., Harrington, I.A., Heffner, R.S., and Heffner, H.E. (2002). Behavioral audiograms of homozygous med(J) mutant mice with sodium channel deficiency and unaffected controls. *Hear. Res.* 171, 111–118. [https://doi.org/10.1016/s0378-5955\(02\)00492-6](https://doi.org/10.1016/s0378-5955(02)00492-6).
108. Brunner, C., Grillet, M., Urban, A., Roska, B., Montaldo, G., and Macé, E. (2021). Whole-brain functional ultrasound imaging in awake head-fixed mice. *Nat. Protoc.* 16, 3547–3571. <https://doi.org/10.1038/s41596-021-00548-8>.
109. Li, S.-B., Borniger, J.C., Yamaguchi, H., Hédou, J., Gaudillière, B., and de Lecea, L. (2020). Hypothalamic circuitry underlying stress-induced insomnia and peripheral immunosuppression. *Sci. Adv.* 6, eabc2590. <https://doi.org/10.1126/sciadv.abc2590>.
110. Stelzer, I.A., Ghaemi, M.S., Han, X., Ando, K., Hédou, J.J., Feyaerts, D., Peterson, L.S., Rumer, K.K., Tsai, E.S., Ganio, E.A., et al. (2021). Integrated trajectories of the maternal metabolome, proteome, and immune predict labor onset. *Sci. Transl. Med.* 13, eabd9898. <https://doi.org/10.1126/scitranslmed.abd9898>.
111. Zunder, E.R., Finck, R., Behbehani, G.K., Amir, E.A.D., Krishnaswamy, S., Gonzalez, V.D., Lorang, C.G., Bjornson, Z., Spitzer, M.H., Bodenmiller, B., et al. (2015). Palladium-based mass tag cell barcoding with a doublet-filtering scheme and single-cell deconvolution algorithm. *Nat. Protoc.* 10, 316–333. <https://doi.org/10.1038/nprot.2015.020>.
112. Finck, R., Simonds, E.F., Jager, A., Krishnaswamy, S., Sachs, K., Fantl, W., Pe'er, D., Nolan, G.P., and Bendall, S.C. (2013). Normalization of mass cytometry data with bead standards. *Cytometry A* 83, 483–494. <https://doi.org/10.1002/cyto.a.22271>.

## STAR★METHODS

## KEY RESOURCES TABLE

REAGENT or RESOURCE	SOURCE	IDENTIFIER
Chemicals, peptides, and recombinant proteins		
Ibuprofen sodium salt	Millipore Sigma	CAS# 31121-93-4
Rhodamine B isothiocyanate dextran dye	Sigma-Aldrich	MDL number: MFCD00132176
Experimental models: Organisms/strains		
C57BL/6J mice	The Jackson Laboratory	RRID: IMSR_JAX:000664
Bacteria and Virus strains		
GCaMP6s virus	Addgene	N/A
AAV.CamKII.GCaMP6s.WPRE.SV40	Addgene	107790-AAV9
pAAV-Ef1a-fDIO-GCaMP6s	Addgene	105714-AAV8
pAAV-mDlx-GCaMP6f-Fishell-2	Addgene	83899-AAV9
pAAV-hSyn-ChRmine-mScarlet-WPRE	Addgene	130994
Software and algorithms		
ImageJ	<a href="https://imagej.net/ij/">https://imagej.net/ij/</a>	N/A
Python	<a href="https://www.Python.org/">https://www.Python.org/</a>	version 3.11
Graphpad prism	<a href="https://www.graphpad.com">https://www.graphpad.com</a>	version 9
Other		
Hydrophone	Onda Corporation	HGL 0200

## RESOURCE AVAILABILITY

## Lead contact

Further information and requests for the resources should be directed to and will be fulfilled by the lead contact, Luis de Lecea ([llecea@stanford.edu](mailto:llecea@stanford.edu)).

## Materials availability

This study did not generate new unique reagents.

## Data and code availability

- All data reported in this paper will be shared by the lead contact upon reasonable request.
- Photometry and behavioral data have been deposited at the Harvard Dataverse repository and are publicly available (<https://doi.org/10.7910/DVN/PCWRAD>).
- Photometry analysis software used<sup>16</sup> can be found on the PhoCUS dedicated Github repository ([https://github.com/keith-orca/usp\\_analysis](https://github.com/keith-orca/usp_analysis)) and part files for 3D printing can be found at the following CAD file repository (<https://www.tinkercad.com/things/2MZM0U9srGP-phocus-parts>). Original custom behavioral tracking code is available in this paper's supplemental information.
- Any additional information required to reanalyze the data reported in this paper is available from the lead contact upon request.

## EXPERIMENTAL MODEL AND SUBJECT DETAILS

For experiments wild type and transgenic male and female adult mice (*Mus musculus*) between 8 and 40 weeks of age, which were group housed in plexiglass chambers at constant temperature of  $22 \pm 1^\circ\text{C}$  and 40–60% humidity, under a normal circadian light–dark cycle (lights-off 7 a.m., lights-on at 7 p.m.). Food and water were available to animals *ad libitum*. All experiments were performed in accordance with the guidelines described in the US National Institutes of Health *Guide for the Care and Use of Laboratory Animals* and approved by Stanford University Administrative Panel on Laboratory Animal Care. For photometry experiments, the following strains were used as indicated: C57BL/6J (JAX Strain #000664), TH-FlpO::B6. For cell type specific GECI expression, the following 400 nL of the following AAVs were injected in the brain area of interest: TH-FlpO::B6 (LC); FpAAV-Ef1a-fDIO-GCaMP6s, C57BL/6J (CMT); AAV.CamKII.GCaMP6s.WPRE.SV40, C57BL/6J (BNST); DLX pAAV-mDlx-GCaMP6f-Fishell-2.

**METHOD DETAILS**

Stereotactic virus injection and fiber optic implant were performed consecutively within a single surgical procedure. Mice were anesthetized with a ketamine xylazine cocktail (100 and 10 mg/kg, intraperitoneal; i.p.) and head mounted within a stereotaxic frame (David Kopf Instruments, Tujunga, CA). To express viral constructs, we infused virus through a stainless steel 28-gauge internal microinjector (Plastics One, Inc., Roanoke, VA) connected to a 10- $\mu$ L Hamilton syringe. Fiber optic cannula with a 2 mm housing O.D. and a 400  $\mu$ m fiber core (0.48 NA; Doric Lenses), were first marked along the cannula at exactly 5.5 mm from the fiber tip to indicate the distance from transducer face to the ultrasound focus. The fiber was then implanted immediately above the target brain region of interest and dental cement was formed around the cannula and skull up until the marking to create a ledge where the ultrasound transducer would be stopped along the z-positioning axis. A dummy transducer was then secured to the coupling agent bracket and mounted to the cannula. The bracket was then carefully secured using dental cement without covering the adjacent skull surface with additional dental cement. We used the following stereotactic coordinates (in mm): Central Medial Thalamus ( $-1.27$  A/P,  $\pm 0.4$  M/L,  $-4.5$  D/V for virus;  $-4.4$  D/V for fiber optic). Dorsomedial hypothalamus ( $-1.8$  A/P,  $\pm 0.4$  M/L,  $-4.9$  D/V for virus;  $-5.1$  D/V for fiber optic). Lateral hypothalamus ( $-1.35$  A/P,  $\pm 1.0$  M/L,  $-5.15$  D/V for virus;  $-5.3$  D/V for fiber optic implants), Locus Coeruleus ( $-5.45$  A/P,  $\pm 1.05$  M/L,  $-3.4$  D/V for virus;  $-3.2$  D/V for fiber optic), Bed nucleus stria terminalis ( $0.1$  A/P,  $\pm 0.88$  M/L,  $-3.8$  D/V for virus;  $-4.0$  D/V for fiber optic). Animals were After surgery, mice were given buprenorphine-SR (1 mg/kg, subcutaneously) once prior to surgical implantation, and every 48–72 h as needed. Mice were given at least 7 days to recover prior to experimentation.

**Histological imaging**

Mice were anesthetized through i.p. injection of ketamine and xylazine (100 and 10 mg/kg, respectively, i.p.) and transcardially perfused with 8 mL phosphate buffered saline (PBS), followed by perfusion with 8 mL paraformaldehyde (4%, in PBS). Brains were extracted and fixed for 12–18 h in 4% PFA at 4°C, and cryoprotected for at least 48 h at 4°C in sucrose solution (30% sucrose in PBS containing 0.1% NaN3). Brains were sliced in 30  $\mu$ m coronal sections at  $-21^{\circ}$ C on a Leica Microsystems cryostat, collected in 24 well plates containing PBS with 0.1% NaN3, and stored at 4°C in darkness until imaging. Sections were mounted on gelatin-coated glass slides (FD Neurotechnologies, Inc.; PO101), and mounted with coverslips and a thin layer of Fluoroshield containing DAPI Mounting Media (Sigma; F6057). Images were collected on a Zeiss LSM 710 confocal microscope (Hebron, KY) with ZEN software, and minimally processed using ImageJ (NIH) to enhance brightness and contrast for visualization purposes.

**Focused ultrasound parameter examination**

For parameter optimization experiments, animals were gently scruffed and the fiber optic patch cable was threaded through the transducer stack and coupled to the cannula. Ultrasound transducer silicone grease was loaded into the gel coupling bracket using a small gel applicator stick. The transducer stack was then mounted to the cannula and lowered into the coupling agent; the grease should flow outside of the bracket ports, indicating the chamber is full. The set screw is turned until snug and holding the stack in place. Animals were left to habituate with *ad libitum* food and water access for 18–24 h before the experimental recording. All experiments were performed between ZT 1–11 during the light cycle. Ultrasound delivery was performed as described previously, using a 550 kHz operating frequency (Figure S1) with the parameters described in Table S1. For parametric examinations, each combination was trialed 7 times in randomized order for each animal with a 3-min interval between the beginning of each trial.

**Fiber photometry data collection and analysis**

Ultrasound waveforms were controlled using the PhoCUS system.<sup>16</sup> Data were collected using a Neurophotometrics FP3002 system and  $\Delta F/F$  were performed as described as previously.<sup>16</sup> GCaMP6s and UV autofluorescence channels were collected for all standard photometry experiments. Rhodamine B isothiocyanate dextran dye experiments included collection of red fluorescence. Photometry channels were sampled at 32Hz and smoothed with a moving average window (5 reads (156 ms)). Protocol sets were delivered regularly in a randomized order using the NumPy random permutation function to prevent chain-effects. The photometry signals were first converted to  $\Delta F/F$  by calculating the average F over the individual trial baseline period prior to stimulation onset using the following equation.

$$\frac{\Delta F}{F} = F \left( \frac{F - \text{base}}{\text{base}} \right) * 100$$

Where **F** is a fluorescence value and **base** is equal to the mean fluorescence value over a given baseline period. The baseline was considered any time prior to a stimulus onset for a given trial.

Due to variant GECI expression across animals, the dynamic range of the  $\Delta F/F$  varies substantially without representing true differences in neural activity range. Thus, trial values were normalized to mean absolute signal variation within each experiment using the following equation.

$$F_i^{\text{Norm}} = \frac{F_i}{\sum_{i=1}^N / N}$$

Where  $i$  is a single fluorescence value,  $N$  is the total number of values across an experiment, and  $||$  indicates a conversion to an absolute value.

UV correction was applied to GCaMP6s by subtracting the UV  $\Delta F/F$  signal from the blue signal. Rhodamine B isothiocyanate dextran dye exhibited a non-linear decay as expected from renal clearance. To correct for this, an exponential decay function was defined as  $y = a \times e^{-kx} + b$ , where  $x$  represents the time or index,  $a$  is the amplitude,  $k$  the decay constant, and  $b$  the baseline offset. Data fitting was executed using the `curve_fit` function from the `scipy.optimize` module, employing non-linear least squares to optimize the parameters  $a$ ,  $k$ , and  $b$  with initial guesses set to  $(1, 0, 1)$ . The optimized parameters were used to generate a fitted signal, which was then subtracted from the Rhodamine B dextran signal.

#### Brain temperature monitoring

Temperature probes were constructed from PFA-insulated 70  $\mu\text{m}$  diameter K-type thermocouple wire (Omega, part# 5TC-TT-K-40-36). Insulation was stripped at the ends of the wires and the brain-contacting wires were twisted and cut, yielding a short junction segment (<0.5 mm of exposed metal) to sample temperature. The other wire ends were crimped to gold-plated connectors (Eaton, part#220-P02-100). A probe was super-glued parallel to the side of the glass fiber of a standard photometry optical probe, with the exposed end extending <1 mm past the fiber tip. For implantation, the photometry probe (cannula and silica fiber) was implanted in the CA1 following the standard surgical procedure outlined above. For the subcranial probe, a 0.5 mm diameter hole was drilled in the skull at the following coordinates: 2.3 AP, -0.5 ML, 1.3 DV; this region of the skull is directly underneath the radiating surface of the transducer. The probe was then slotted underneath the skull to be positioned directly above the brain and secured with dental cement. Thermocouples were implanted and a DC amplifier (Brownlee model440) was used to amplify voltage signals X1000, which was digitally sampled at 5kHz (National Instruments). Voltage vs. temperature linear fits were generated in a water bath with a liquid-in-glass thermometer, ranging from 0°C to 60°C, to calibrate brain temperature readings before and after the experiment.

#### Peripheral auditory brainstem response prediction

The auditory brainstem response (ABR) is not a direct measure of audibility, but rather a measure of sharp changes in audibility. ABR following FUS stimulation was predicted based on the methods described in Choi et al.<sup>59</sup> Briefly, the signal that reaches the cochlea was assumed to be the time-varying Fourier components of the square of FUS signal pressure. Since the changes in basilar displacement are neuronally encoded with the animal's hearing sensitivity in consideration, the Fourier components were differentiated over time and scaled by the inverse of ABR thresholds of mice. The resulting function was convolved with the ABR impulse response function-based Ohm's acoustic law to obtain the final ABR prediction.

#### Audible tone response

An Agilent 33220A function generator was connected directly to a single piezoelectric tweeter (model # Piezo-KS-3840A-2P-RE) hanging inside the animal's cage. The horn was set to deliver 16kHz sound at 2.5 Hz, 10% duty cycle for 10 s (400 ms burst interval, 640 cycles per burst, 600 mV). The flat response dB(Z) measured at 16 kHz was 96.4, as compared to ~18 dB ambient, using the Decibel-X application with the microphone placed facing the piezo speaker from the bottom of the animal's cage. 16 kHz is approximately the peak hearing frequency of mice<sup>107</sup> and the sound produced was clearly audible to the experimenter at a distance from the cage.

#### Optical excitation and inhibition

For optogenetic stimulation, the DMH was injected with AAV-Syn-Chrmire 200 nL with an optical fiber implanted above the sight. The PhoCUS probe was coupled to match conditions of the ultrasound behavioral experiments. 560 nm light was delivered for 10 s every 3 min (0.5 mW, 50 ms pulses, 10 hz).

#### Motion, stretch attend posture, and body temperature quantification

Animals were connected to the PhoCUS probe and briefly habituated (30–40 min) and recorded during lights on (ZT 0–12) except for inhibitory protocol examination (Figure 3B) performed during the dark phase to ensure animal movement post-habituation (ZT 12–24). An FLIR lepton thermal camera was used to capture images at ~8 fps. Background intensity was normalized by linearly correcting all pixels in each image such that image background (mode) was 23°C. Dynamic blob detection was performed with a threshold of 27°C, providing an outline the animal's body (Video S1). For tracking location, the peak value was used which was typically positioned over the BAT tissue area. We performed stretch-attend posture detection as described previously.<sup>64</sup> Briefly, the animal's contour was outlined for each frame and fit with an ellipse using the OpenCV library. The longest axis along the ellipse was then calculated with the end nearest the peak temperature labeled as "head" and the opposite end "tail". The eccentricity of the ellipse was used to create a Boolean array where any 4+ consecutive frames (~0.5 s) where the animal's elliptical eccentricity was greater than 0.9 and the animal's speed was <2 pixels were given a value of 1 for SAP. Head and tail speed were calculated for each frame. Walking speed was quantified as a non-zero value when both the head and tail were in motion. Head speed was quantified as a non-zero value when head, but not tail movement was detected (See supplemental code).

**Rotarod task**

Prior to experimentation, animals were required to complete three training sessions on the rotarod. Animals were required to stay on the rotarod for two sessions with linearly increasing speed from 10 to 60 (acceleration of +1 rpm/second) and subsequently required to stay on the rotarod at a speed of 16 rpm for at least 10 s. Animals were given 3 min rest between all trials. For each test trial, stimulus was delivered if animals were able to stay on the rotarod for at least 5 s; falls before 5-s in the absence of stimulation were considered mistrials. Rotarod failure time was automatically captured using an infrared beam which is broken when an animal drops off the rod and onto the floor. Failure time was manually marked when an animal holds immobile to the rotarod and makes one-half rotation to the underside of the apparatus.

**Blood volume quantification**

Rhodamine B isothiocyanate dextran dye (Sigma, R9379 10 or 70 kDa) was dissolved in saline at a concentration of 10 mg/mL 100  $\mu$ L was injected retro-orbitally under light isoflurane anesthesia. Following 10 min anesthesia recovery, fiber photometry collection was started. 100  $\mu$ L was injected retro-orbitally under light isoflurane anesthesia. Animals were quickly mounted to a head-bar bracket while under anesthesia and allowed to recover from anesthesia for 10 min prior to imaging. For COX-2 inhibition, the experiments were repeated with I.P. injection of either saline (vehicle), or ibuprofen (100 mg/kg in saline, Millipore Sigma CAS# 31121-93-4) 30 min prior to rhodamine dye injection-based blood volume monitoring. The decaying level of rhodamine in the blood was corrected for by fitting an exponential decay function  $f(x) = a * e^{-kx} + b$  (NumPy:  $a * np.exp(-k*x) + b$ ), where  $x$  represents time,  $a$  represents the initial amplitude,  $k$  represents the decay rate, and  $b$  represents the baseline offset. The exponential decay model was fit using the `scipy curve_fit` function with an initial guess of parameters ( $p0 = (1, 0, 1)$ ).

**Ultrafast power Doppler imaging**

Prior to experiments, mice were implanted with an acoustically transparent cranial window as described by Brunner et al.<sup>108</sup> Briefly, animals were anesthetized with 1.5–2.5% isoflurane and placed in a stereotaxic frame (David Kopf Instruments, Tujunga, CA). After removal of the skin, a custom-made titanium headpost was fixed to the skull with Vetcold (3M, Maplewood, Minnesota, USA) and dental cement (C&B Metabond, Parkell, Edgewood, New York). A micro drill (51449; Stoelting Co, Wood Dale, IL, USA) was used to drill the perimeter of the cranial window from AP +2.0 mm to –4.0 mm relative to bregma and sterile saline was regularly applied to cool the skull. After sufficient thinning, the skull fragment was covered with sterile saline and carefully removed with angled forceps, leaving the dura intact. Finally, an acoustically transparent polymethylpentene membrane (ME311051, Coraopolis, Pennsylvania) was sealed to the cranial window using dental cement. Mice were given Carprofen (5 mg/kg, i.p.) once preoperatively and postoperatively for 48–72 h as needed. Animals were allowed at least 7 days of recovery before experimentation.

For the experiments, mice were anesthetized with 2.5% isoflurane, connected to a 3D-printed head clamp with and placed on a heating pad to maintain a body temperature of 37.0°C. Isoflurane was reduced to 1.0% and the cranial window was covered with sterile saline and degassed ultrasound gel. A single element 500 kHz transducer (H204, Sonic Concepts, Bothell, WA, USA) with a 15 MHz linear array (L22-14vXLF, Vermon, S.A., Tours, France) confocally aligned with the annular opening of the FUS transducer was positioned above the cranial window using a 3D-motorized positioning system (BiSlide; Velmex, Bloomfield, NY, USA). The transducers were coupled to ultrasound gel on top of the cranial window with a degassed water filled cone and the coupling preparation was held at a temperature of 36°C (measured at the cranial window) using heating elements. Experiments ( $n = 5$  mice) consisted of 4 trials with a 25 s baseline, 5 s sonication and a 155 s cooldown period. FUS (pressure = 0.767 MPa, intensity = 18.89 W/cm<sup>2</sup>, pulse duration = 80 ms, duty cycle = 20%) was delivered to the CMT at 3 mm posterior to the center of the natural focus. Pressure and intensity of the FUS transducer were calibrated prior to the experiments using an HGL 0200 hydrophone (Onda Corporation, Sunnyvale, CA, USA) in degassed water.

Power Doppler Imaging was performed in the coronal plane with a custom imaging sequence generated with a research ultrasound system (Vantage 256, Verasonics, Kirkland, WA) as previously described.<sup>75</sup> Briefly, plane waves were sent at 9 angles evenly spaced from –6° to +6°. At each angle, 3 plane waves were averaged internally in the research ultrasound system. Plane waves were transmitted at 13500 Hz resulting in a compounded frame rate of 500 Hz. After each acquisition of 70 compounded frames, the data were beamformed (delay and sum) and filtered with singular value decomposition (lowest 10% of singular values removed) to remove stationary tissue signal, resulting in a cerebral blood volume (CBV) image. To avoid interference between FUS and power Doppler imaging an interleaved sequence was used, whereas FUS was triggered after an acquisition of power Doppler images and beamforming was completed during FUS. The final frame rate of power Doppler imaging was set to 2.5 Hz and CBV images were acquired over the entire period of each experiment. For processing, CBV images were filtered with a median filter (3x3 pixels) in the spatial domain and a rolling average (2 s window, 5 frames) in the temporal domain. Following this, the CBV signals of each pixel were converted to  $\Delta$ CBV/CBV by calculating the average CBV over the individual trial baseline period before stimulation onset using the following equation.

$$\frac{\Delta CBV}{CBV} = CBV \left( \frac{CBV - base}{base} \right) * 100$$

Where **CBV** is a blood volume value and **base** is equal to the mean cerebral blood volume value over the 25 s baseline period.

After averaging over the 4 trials, regional changes in CBV over time for each animal were calculated by averaging the  $\Delta$ CBV/CBV over manually segmented brain regions according to the Allen Mouse Common Coordinate Framework.

**Corticosterone ELISA**

Plasma was harvested by centrifuging retroorbitally collected, heparinized whole blood for 10 min at 12,000 rpm within 30 min of blood draw, and stored at  $-80^{\circ}\text{C}$  until further processing. The DetectX Corticosterone ImmunoAssay ELISA (multi-species, ArborAssays, MI) was performed according to the manufacturer's instructions. In brief, plasma was diluted 1:500 in dissociation buffer, and duplicates incubated in pre-coated microtiter plates holding conjugate and polyclonal antibody, after which substrate was added to readout the corticosterone concentration at 450 nm against a standard curve generated in the same experiment.

**Single-cell mass cytometry****Ex vivo immunoassay**

Whole blood was collected via retro-orbital bleed into a heparinized tube, and processed within 30 min after draw. Samples were processed using a standardized protocol for fixing with proteomic stabilizer (Smart Tube, CA) and stored at  $-80^{\circ}\text{C}$  until further processing.

**Mass cytometry sample processing, barcoding, and antibody staining**

A 46-parameter mass cytometry antibody panel, targeting extra- and intracellular proteins indicative of phenotype and functional status, was used according to prior protocols.<sup>109,110</sup> Antibodies were either obtained preconjugated (Standard Biotools, CA) or purchased as purified, carrier free (no BSA, gelatin) versions, which were then conjugated inhouse with trivalent metal isotopes utilizing the MaxPAR antibody conjugation kit (Standard Biotools, CA). Samples were barcoded using a 3-out-of-6 Palladium-isotope ( $\text{Pd}^{102-110}$ ) combinatorial strategy.<sup>111</sup> After incubation with Fc block (Biolegend, CA), pooled barcoded cells were stained with surface antibodies, then permeabilized with methanol and stained with intracellular antibodies. All antibodies used in the analysis were titrated and validated on samples that were processed identically to the samples used in the study. To minimize the effect of experimental variability on mass cytometry measurements between serially collected samples, the complete set of samples were processed, barcoded, pooled, and stained simultaneously, and run on the mass cytometry instrument in one acquisition session (Helios CyTOF, Standard Biotools, CA).

**Processing of raw mass cytometry files**

The mass cytometry data (.fcs files) was normalized using Normalizer v0.1 MATLAB Compiler Runtime (MathWorks).<sup>112</sup> Files were then de-barcoded with a single-cell MATLAB debarcoding tool.<sup>111</sup> Manual gating was performed using cloud-based software CellEngine (<https://immuneatlas.org/>) (CellCarta, Montreal, CAN).

**Derivation of cell frequency, and intracellular signaling response features**

A total of twenty-six innate and adaptive immune cell subsets were identified. Cell frequencies were expressed as a percentage derived from singlet, live polymorphonuclear and mononuclear leukocytes ( $\text{DNA}^+ \text{cPARP}^- \text{Ter115}^- \text{CD45}^+$ ). Endogenous intracellular signaling activities were quantified for phosphorylated (p)STAT1, pSTAT3, pSTAT5, nuclear factor kB (pNF-kB), and total inhibitor of NF-kB (IkB), prpS6, pMAKPAPK2, pERK1/2, pP38, and pCREB using an arcsinh-transformed value calculated from the median signal intensity per population.

**QUANTIFICATION AND STATISTICAL ANALYSIS**

Sample sizes were based on what is conventional for the field and previous literature. Comparisons were within subjects or across conditions as noted in the text. Data are presented as mean values accompanied by the Standard Error of the Mean (SEM) except for box and dot plots as noted in figure legends. GraphPad Prism 9 software was used for statistical analyses including standard error of the mean and  $p$  values. Statistical test details for display items can be found in the figure legends. One-sample t test, unpaired two-tailed t test, two-tailed Pearson correlation, repeated-measures ANOVA, with Dunnett's multiple comparison test, and paired two-tailed t test were used when appropriate. The Python import statsmodel glm package was used to perform a two-way ANOVA was used to statistically examine overall effects of brain region, PRF, and temporal compression on brain region response; degrees of freedom, F, and  $p$  values were reported directly in the main text. For all experiments, the null hypothesis was rejected at the  $p < 0.05$  level.